Skin Collagen Reduction Drives Selective Aspects of Aging in Sensory Neurons

Meera M. Krishna[1,2], Ariel L. Franitza[2], Lezi E[1,2,*]

[1]Department of Cell Biology, Neurobiology and Anatomy, Medical College of Wisconsin, 8701 W Watertown Plank Road, Milwaukee, WI 53226, United States of America

[2]Neuroscience Research Center, Medical College of Wisconsin, 8701 W Watertown Plank Road, Milwaukee, WI 53226, United States of America

[*]Corresponding author/Lead contact:
lezie@mcw.edu
+1-414-955-2248

Running Title: Skin Collagen Reduction Drives Neuronal Aging

ABSTRACT

Despite significant progress in revealing molecular and cellular changes in aging nervous system, the upstream mechanisms driving these changes remain elusive. Here, we investigate the regulatory roles of non-neural tissues in neuronal aging, using the cutaneous PVD polymodal neuron in *Caenorhabditis elegans* as a model. We demonstrate that during normal aging, PVD neurons progressively develop excessive dendritic branching, functionally correlated with age-related proprioceptive deficits. Our study further uncovers that decreased skin collagen expression, a common age-related phenomenon across species, triggers PVD aging. Specifically, loss-of-function mutations or adulthood-specific knockdown of *dpy-5* or *col-120*, both genes coding for cuticular collagens secreted to the epidermal apical surface, induce early-onset excessive dendritic branching in PVD, and proprioceptive deficits. Overexpressing *dpy-5* or *col-120* mitigates excessive branching without affecting lifespan, suggesting that skin collagens promote healthspan rather than longevity. Notably, these collagens are not involved in aging-associated dendritic beading, another PVD neurodegenerative phenotype distinctively associated with a different mechanosensitive dysfunction. Skin collagens also specifically affect branching in select sub-classes of sensory neurons. Lastly, we identify *rig-3*, a neuronal Immunoglobulin Superfamily member not expressed in PVD, functioning in the same pathway as skin collagen genes to preserve PVD dendritic integrity during aging. These findings reveal an important causative role of age-related skin collagen reduction in neuronal aging, independent of their traditionally recognized involvement in direct structural support for neurons. Our study offers new insights into understanding selective neuron vulnerability in aging and age-related diseases, emphasizing the need for multi-tissue strategies in addressing the complexities of neuronal aging.

Key Words: Aging; neuronal aging; sensory neurons; collagen; skin; *Caenorhabditis elegans*

1. INTRODUCTION

Age represents a significant risk factor for many neurological disorders, including peripheral neuropathies (Bouche, 2020; Hicks et al., 2021; Martyn & Hughes, 1997; Verghese et al., 2001). While several factors such as diabetes, autoimmune diseases, physical injury, and vitamin imbalances can contribute to neuropathies, aging not only increases susceptibility to these conditions but also raises the prevalence of idiopathic neuropathies (Castelli et al., 2020; Hicks et al., 2021; Watson & Dyck, 2015). Currently, our ability to treat neuropathies in elderly populations is limited, largely due to gaps in our understanding of the mechanisms driving aging of the nervous system. Signaling from non-neural tissues may be a promising avenue to address this gap.

Appropriate signaling from adjacent non-neural tissues, such as the skin, plays an important role in the development of the peripheral nervous system. Studies have shown that overexpression of neurotrophin-4 in the epidermal basal cells of mice leads to abnormally increased sensory endings in the dermal footpad, suggesting that proper expression of neurotrophic factors in the skin is crucial for guiding sensory innervation (Goodness et al., 1997; Krimm et al., 2006). Similarly in *C. elegans*, the morphogenesis of the PVD neuron, a cutaneous sensory neuron with an elaborate dendritic arbor, relies on the cell-adhesion molecule SAX-7 on the skin and several other extracellular proteins, which serve as precise tracks for accurate dendritic arborization (Dong et al., 2013; Salzberg et al., 2013; Yang & Chien, 2019; Ziegenfuss & Grueber, 2013). Epidermal ensheathment is a process where epidermal cells wrap around growing neurites of sensory neurons to regulate branching morphogenesis, which is also highly dependent on two-way signaling between the neuron and the skin; blocking epidermal sheath formation in *Drosophila* and zebrafish results in destabilized dendrite branches and reduced nociceptive function (Jiang et al., 2019). However, whether non-neural tissues also actively contribute to the aging of the peripheral nervous system remains less understood.

During aging, neurons undergo progressive structural deterioration, leading to increased synapse loss and impaired neuronal signal transmission, ultimately resulting in a variety of behavioral abnormalities (Correia et al., 2016; Hunter et al., 2016; Valdez, 2019; Verdú et al.,

2000). Neuritic beading, also known as focal swelling, is an evolutionarily conserved aging-associated structural change indicative of neurodegeneration (Takeuchi et al., 2005; Tan et al., 2007). These neuritic beads, often consisting of broken-down cytoskeletal and motor protein components, can disrupt organelle transport, such as mitochondrial trafficking, leading to bioenergetic dysfunction and eventual neuronal death (Suzumura, 2009; Takeuchi et al., 2005). Our previous research in *C. elegans* has shown that age-related upregulation of antimicrobial peptides in the skin causatively triggers dendritic beading in PVD neurons accompanied by a mechanosensitive functional decline, demonstrating a significant role for skin-derived molecular cues in sensory neuron aging (E et al., 2018).

Increased aberrant neurite branching is another aging-associated structural change in neurons, documented in the peripheral nervous systems of aged rats and elderly human patients with sensory neuropathies (Lauria et al., 1999; Rosenheimer & Smith, 1985; Thomas et al., 2023). While it has been speculated that the increased branching may compensate for other aging-associated structural and functional losses, this counterintuitive phenomenon is not well understood. Interestingly, *C. elegans* PVD neurons also exhibit a pronounced increase in dendritic branching at advanced ages, as briefly mentioned in our prior work (E et al., 2018) and also observed in a separate study by Kravtsov et al. (Kravtsov et al., 2017), though the functional implications and precise underlying mechanisms remain unknown. However, it is noteworthy that the aging-associated excessive branching, unlike the dendritic beading, does not appear to be regulated by skin antimicrobial peptides, suggesting the involvement of alternative mechanisms.

In this study, we provide an in-depth characterization of aging-associated excessive dendritic branching in PVD neurons, demonstrating its functional relevance to age-related decline in proprioception. Using PVD neuron as a model, we further discover that mutations or downregulation of two skin collagen genes, *dpy-5* and *col-120*, induce early-onset excessive dendritic branching and proprioceptive deficits, suggesting that age-dependent reduction of skin collagens plays a causative role in sensory neuron aging. Moreover, overexpression of these collagen genes mitigates the severity of excessive branching in aged animals. Importantly, our results also indicate that the regulatory role of skin collagens is specific to branching integrity during aging and is limited to certain types of cutaneous sensory neurons.

Additionally, we identify RIG-3, a neuronal Immunoglobulin Superfamily protein, as a partner in skin collagen's regulation of PVD dendritic integrity. These findings reveal a novel role for skin collagens in actively regulating sensory neuron aging, expanding our understanding of the upstream molecular mechanisms that drive nervous system aging.

2. RESULTS

2.1 Aging triggers the progressive development of excessive higher-order dendritic branching in PVD sensory neurons

To investigate how skin tissues may affect the aging of sensory neurons, we employed the PVD polymodal neuron of *C. elegans* as our experimental model. The PVD neuron is a cutaneous multi-dendritic mechanosensory neuron that spans the entire body of the animal along the anterior-posterior axis excluding the head, neck, and tail (Oren-Suissa et al., 2010; Tsalik et al., 2003). Functionally, the PVD is involved in harsh touch sensation, cold sensation, and proprioception (Chatzigeorgiou et al., 2010; Tao et al., 2019). Each animal possesses two PVD neurons, PVDR on the right and PVDL on the left (Smith et al., 2010; Way & Chalfie, 1989). The dendritic branches of the PVD neuron extend dorsally and ventrally, with a singular axon that synapses ventrally with the AVA and PVC interneurons (Fig. 1A) (Smith et al., 2010; Way & Chalfie, 1989; White et al., 1986). From the PVD soma, two primary (1°) dendritic branches extend in the anterior and posterior directions, respectively, with secondary (2°) dendrites emerging orthogonally from the 1° dendrites at regular intervals, forming non-overlapping 'menorah-like' repeating units mainly composed of tertiary (3°) and quaternary (4°) dendrites (Fig. 1B) (Halevi et al., 2002; Oren-Suissa et al., 2010; Smith et al., 2010). The normal aging process of PVD neurons, as previously investigated by our group and others (E et al., 2018; Saberi-Bosari et al., 2020), often involves the progressive development of bead-like structures along the dendrites (Fig. S1A), resembling morphological changes observed in human patients with peripheral neuropathies or mammalian models of age-related neurodegenerative diseases (Ashford et al., 1998; Faerman et al., 1982; Jin et al., 2011; Lauwers et al., 2003; Menzies et al., 2015; O'Donnell et al., 2014). We have demonstrated that the majority of the beading structures in PVD dendrites indicate a disrupted microtubule

network and are associated with age-related deficits in the harsh touch sensing function of PVD neurons (Fig. S1B) (E et al., 2018).

In this study, we focused on another distinctive aging phenotype of PVD neurons – excessive dendritic branching, previously noted in literature (E et al., 2018; Kravtsov et al., 2017) yet lacking clarification regarding its functional implications and underlying mechanisms. We first conducted a thorough characterization of this phenotype throughout the normal aging process of control animals [*wdIs51* (*F49H12.4::GFP)*]. Our analysis revealed a progressive and substantial increase in the number of 5° and 6° dendritic branches from Day 1 to Day 9 of adulthood (Fig. 1C-E, Fig. S1C-F), while the number of 4° dendrites or PVD menorahs remained unchanged (Fig. S1G-N). Notably, no age-related ectopic branching was detected in the axons. To ascertain whether the observed excessive dendritic branching is an inherent consequence of aging, we pursued a different approach from the common method of disrupting specific aging signaling pathways, such as *daf-2* signaling (Kenyon, 2010). Instead, we leveraged the well-established correlation between environmental temperatures and the aging process in *C. elegans*. Previous studies have demonstrated that higher temperatures accelerate aging, while lower temperatures decelerate it, potentially involving multiple signaling pathways (Chen et al., 2019; Klass, 1977; Lee & Kenyon, 2009; Vakkayil & Hoppe, 2022; Xiao et al., 2013). Our findings revealed a temperature-dependent variation in the severity and progression of PVD dendritic branching (Fig. 1F-G), suggesting that this morphological change is an intrinsic aspect of aging. Furthermore, our analysis indicated that the significant increase in branching persisted even after adjusting for the slight increase in body length during aging (Fig. S1W-X), further reinforcing the relevance of this phenotype to aging. Kravtsov et al. previously showed that *daf-2* mutant animals exhibited increased 5°-7° dendritic branches in PVD neurons to a similar extent as control animals of the same advanced ages (Kravtsov et al., 2017), implying that the intrinsic aging nature of this morphological change is independent of the insulin/IGF-1 pathway but potentially involves other aging signaling pathways.

Upon conducting a more in-depth analysis of the aging-associated higher-order (≥ 5°) dendritic branching, we observed that its extent and progression were comparable between left and right PVD neurons throughout aging (Table S1). While slight variations were noted in the number of higher-order branches when comparing the dorsal and ventral sides of PVD

118 neurons, the overall aging-associated trend remained evident in both sides (Fig. S1C-F).
119 Importantly, this trend persisted even after normalization for the number of PVD 'menorah'
120 structures or 4° dendritic branches (Fig. 1H-K, Fig. S1O-R). Furthermore, using the position of
121 the PVD soma as a dividing point, we compared between the anterior and posterior sections.
122 Following a similar normalization approach, although the extent of high-order branching per
123 PVD 'menorah' or per 4° dendritic branches in the posterior section was notably greater than
124 that in the anterior section of the same PVD neuron across ages, the aging-associated
125 increase trend was observed in both sections (Fig 1L-O, Fig. S1S-V).

126 During development, stabilized microtubules are often found in large primary dendrites, while
127 actin is abundant in small higher-order dendrites or dendritic spines, playing a crucial role in
128 anatomical plasticity (Kaech et al., 2001; Stewart et al., 2012). To determine the cytoskeletal
129 composition of the aging-associated higher-order dendritic branches of PVD neurons, we used
130 transgenic strains expressing *ser-2(3)p::EMTB::GFP* (microtubule-binding domain of ensconsin
131 fused to GFP) or *ser-2(3)p::GFP::UtrCH* (calponin homology domain of F-actin binding protein
132 utrophin fused to GFP) to visualize polymerized microtubules or actin filaments, respectively, in
133 PVD neurons (Burkel et al., 2007; Chia et al., 2014; E et al., 2018; Richardson et al., 2014;
134 Shaye & Greenwald, 2015; Tang et al., 2019). *ser-2(3)p::mCherry-PH* was co-expressed in
135 both strains to visualize the membrane structures of PVD dendrites. We found that
136 microtubules were not detectable in >3° dendritic branches in aged control animals (Fig. S2A),
137 similar to the microtubule distribution pattern in young adults (Liu et al., 2019). In line with
138 previous reports (Tang et al., 2019), our time-lapse imaging analysis of young adult control
139 animals showed abundant localization of F-actin in 4° dendrites and the leading edges of
140 occasional higher-order dendritic branches (Fig. 1P, Fig. S2B). Interestingly, the excessive
141 5°/6° dendrites in aged control animals primarily consisted of F-actin as well (Fig. 1P, Fig.
142 S2B). Further quantitative analysis of our time-lapse imaging data indicated dynamic
143 remodeling of F-actin-rich higher-order branches in both young and aged control animals, with
144 frequent outgrowths and retractions over minutes (Fig. 1Q-R). Notably, within the same
145 observation period, higher-order branches in aged control animals tended to gain length, while
146 those in young adults appeared prevented from further growth (Fig. 1S). Given the crucial role
147 of pruning or phagocytosis in neural network refinement during development (Raiders, Han, et
148 al., 2021), it is plausible that this process could also contribute to the dynamic remodeling of

149 higher-order branches during adulthood. In *C. elegans*, both epidermal cells and body wall
150 muscles can take on amateur phagocytic roles (Chiu et al., 2018; Nichols et al., 2016).
151 Typically, phagocytosis results in the presence of cellular debris in the vicinity. However, we did
152 not observe such debris near the remodeled regions, which would theoretically be visible as
153 fluorescent puncta (Raiders, Black, et al., 2021), suggesting that the dynamic remodeling of
154 PVD higher-order branching is unlikely to occur through phagocytosis. Importantly, we did not
155 observe abnormal overlapping of dendritic branches when excessive higher-order branching
156 developed during aging. Previous studies have shown that manipulation of several genes that
157 regulate PVD dendrite self-avoidance during development, such as *mig-14*/Wntless and *eff-*
158 *1*/fusogen, affects 2°- 4° branching but does not seem to affect higher-order branches
159 (Kravtsov et al., 2017; Liao et al., 2018; Oren-Suissa et al., 2010), suggesting that the
160 observed phenotype in our study is also independent of dysregulated self-avoidance between
161 sister dendrites. Collectively, these findings point to potential alternative adulthood-specific
162 regulatory mechanisms that effectively preserve dendritic branching integrity in young adults
163 but may be compromised in aged individuals.

164 **2.2 Aging-associated excessive dendritic branching in PVD neurons correlates with**
165 **proprioceptive deficits**

166 We then explored the potential functional implications of the excessive branching observed in
167 aging PVD neurons. Harsh touch sensation is a well-studied function of PVD neurons; this
168 function relies on their proper synaptic connections with downstream command interneurons
169 that further integrate signals into motor neuron circuits to initiate an escape movement
170 (Chatzigeorgiou et al., 2010; Husson et al., 2012). To examine the relevance of excessive PVD
171 dendritic branching in dysfunctional harsh touch sensation, we first performed the behavioral
172 analysis of noxious harsh touch response (Chatzigeorgiou et al., 2010; E et al., 2018), followed
173 by the examination of the dendrite morphology of the same animal, enabling a within-individual
174 analysis of the correlation between the dendritic structure deterioration and sensory deficits.
175 Interestingly, our findings showed that age-dependent decline of harsh touch response in
176 control animals (E et al., 2018) had no correlations with the extent of PVD higher-order
177 dendritic branching (Fig. S3A), as opposed to the strong positive correlation with aging-
178 associated dendritic beading phenotype (Fig. S1B).

As a polymodal neuron that responds to several distinct sensory modalities besides harsh touch, the integrity of PVD dendritic menorah structures has specifically been shown to be critical in providing proprioceptive regulation, without relying on PVD axons' synaptic function (Albeg et al., 2011; Tao et al., 2019). Proprioception refers to the ability to process sensorimotor input for posture control and precise movement output; with *C. elegans*, it can be assessed by measuring the tracks that the animals leave on agar plates seeded with *Escherichia coli* OP50 (standard food in laboratory maintenance), through their sinusoidal body-bend movements (Fig. 2A) (Tavernarakis et al., 1997). Animals harboring a loss-of-function mutation in *dma-1* or in several other genes that lead to impaired morphogenesis of PVD menorah structures (marked by the absence of dendritic arborization beyond 2° branches) exhibit a decrease in track wavelength and amplitude (Tao et al., 2019). We therefore hypothesized that the excessive higher-order dendritic branching in aging PVD neurons could manifest as proprioceptive deficits at the behavioral level.

To test our hypothesis, we first examined the proprioceptive function in control (CT) animals during aging. Compared to young Day 3 animals, we observed a significant decrease in the mean amplitude and mean wavelength of the sinusoidal movements in aged Day 9 animals (Fig. 2B-C). Additionally, there was a notable increase in within-individual variability in the wavelength of tracks in Day 9 animals, accompanied by a trend towards increased within-individual variability in amplitude (Fig. 2D-E). These age-related changes resemble the gait pattern changes observed in elderly humans, such as decreased stride length/width and greater variability in these parameters, strongly associated with a decline in proprioception (Callisaya et al., 2010; Henry & Baudry, 2019; Ko et al., 2016; Wiesmeier et al., 2015). We then conducted a within-individual correlation analysis between PVD branching severity and proprioceptive function (Fig. 2, Fig. S3). Our analysis revealed that the extent of 'higher-order' branches, dorsal 6º branches in particular, was negatively correlated with the mean amplitude or mean wavelength (Fig. 2F-G). On the other hand, the severity of dorsal 6º branches was positively correlated with the variability in track amplitude or wavelength (Fig. 2H-I). These findings establish a novel link between aging-associated excessive branching of PVD dendrites and age-related proprioceptive deficits.

Subsequent examination of PVD dendritic beading and excessive branching within individual animals revealed an absence of concurrence of these two aging-related phenomena; rather, a negative correlation seems evident, wherein animals exhibiting a pronounced beading phenotype are less likely to exhibit severe branching, and vice versa (Fig. S3V-W). This observation, coupled with our finding regarding the distinct behavioral manifestations of dendritic beading and excessive branching (E et al., 2018) (Fig. 2, Fig. S1B, Fig. S3), further implies that neurons may undergo a variety of morphological changes during aging, each associated with unique functional consequences. Our findings also hint at the existence of a potential compensatory mechanism aimed at preserving certain functions of polymodal neurons.

2.3 Loss-of-function mutations in skin collagen genes lead to an early onset of excessive PVD dendritic branching and proprioceptive deficits

We next investigated the molecular mechanisms underlying the development of aging-associated excessive branching. In our previous research, we identified a skin antimicrobial peptide (AMP) as a factor contributing to PVD dendritic beading; interestingly, this factor does not explain the phenomenon of aging-associated excessive dendritic branching (E et al., 2018). However, it does suggest that age-related changes in the skin can influence the aging of PVD neurons, which motivated us to explore whether other molecular changes in the aging skin could play a role in the observed excessive branching. A prime candidate for such a role is the age-related decline in skin collagen gene expression (Fig. S4A) (GEO accession GSE176088) (Sheng & Xiao, 2021), a phenomenon well-documented in various organisms, including rodents and humans (Fatima et al., 2022; Kehlet et al., 2018; Stammers et al., 2020; Varani et al., 2006). Our exploration into the downregulated skin collagen genes during aging led us to discover that null mutations in either *dpy-5* or *col-120* resulted in an early-onset of the excessive PVD dendritic branching by Day 3 of adulthood, comparable to the branching severity observed in much older control animals (Fig. 3A-G).

In *C. elegans*, the skin is primarily composed of a simple epithelium that secretes a collagenous cuticle to the apical side, creating an additional protective barrier against the environment (Chisholm & Hsiao, 2013; Chisholm & Xu, 2012; Kramer et al., 1988). DPY-5 and

COL-120 are classified as cuticular collagens (Teuscher et al., 2019; Thacker et al., 2006). The highly polarized nature of the *C. elegans* epidermal cells segregates apically secreted cuticular collagens from basement membrane collagens, both anatomically and functionally. This suggests that these cuticular collagens are unlikely to physically interact with sensory neurons located on the epidermal basal side to affect neuronal morphology (Chisholm & Hsiao, 2013; Chisholm & Xu, 2012). Additionally, DPY-5 and COL-120 share a similar domain architecture with mammalian membrane-associated or fibril-associated collagens with interrupted triple-helices (Johnstone, 2000; Ricard-Blum, 2011; Tu et al., 2015), further distinguishing them from basement membrane collagens (Fig. 3A). Moreover, the expression of *dpy-5* and *col-120* are not temporally clustered, and their proteins localize to distinct areas within the apical side of the epidermis (Davis et al., 2022; Teuscher et al., 2024; Thacker et al., 2006), suggesting that they likely do not interact with each other functionally. Importantly, DPY-5 and COL-120 protein levels both decrease with age in wild-type animals (Teuscher et al., 2024; Thacker et al., 2006). Although mutations in either *dpy-5* or *col-120* do not compromise the skin integrity of the animals (Sandhu et al., 2021; Van de Walle et al., 2019), both genes affect body size. *dpy-5 (e907)* mutants are noticeably shorter and wider (Sandhu et al., 2021; Thacker et al., 2006), while *col-120 (sy1526)* mutants appear slightly elongated (Fig. S4C). In addition, both mutants exhibited reduced lifespans (Fig. S4D), suggesting a broader impact on organismal health, potentially due to developmental anomalies. To mitigate the confounding influence of body size changes on our analysis, we normalized dendritic branching to the body length of individual animals. This normalization confirmed that *col-120 (sy1526)* mutants exhibited early-onset 'higher-order' dendritic branching at Day 3, even when adjusted to body size (Fig. S1W-X).

To further solidify the specific role of skin collagens in this phenotype, we performed rescue experiments. The expression of wild-type *dpy-5* cDNA under the control of an epidermis-specific promoter successfully rescued the excessive dendritic branching phenotype in *dpy-5 (e907)* mutants at Day 3 (Fig. 3D-E, additional rescue line in Fig. S4E-F). A similar rescue effect was observed when wild-type *col-120* cDNA was expressed using epidermis-specific promoters in *col-120 (sy1526)* mutants (Fig. 3F-G, additional rescue line in Fig. S4G-H). PVD neurons complete their dendritic arborization around the late L4 stage (last/4th larval stage) (Hess et al., 2019; Liu & Shen, 2011; Smith et al., 2010). Examination of *dpy-5* and *col-120* mutant animals at the L4 stage revealed a slight increase in excessive dendritic branching

compared to control animals, though not reaching the extent observed in Day 3 mutant animals (Fig. S4I-J). To determine whether the excessive dendritic branching observed in *dpy-5* or *col-120* mutants arises from developmental defects or is genuinely associated with aging, we performed adulthood-specific systemic RNA interference (RNAi) knockdowns of these genes. RNAi treatment was initiated at the late L4 stage to avoid interfering with PVD dendritic morphogenesis, and phenotyping was performed 3 days later (Day 3 of adulthood). The effectiveness of adulthood RNAi was validated through RT-qPCR analysis (Fig. S4B). We first confirmed that control animals fed on HT115(DE3) bacteria harboring empty vector L4440 (EV, used as a negative control in RNAi assays) exhibited aging-associated excessive dendritic branching in PVD neurons (Fig. S4K-L), to a similar extent as observed in control animals fed on OP50. Our data show that a modest suppression of *col-120* or *dpy-5* expression via the adulthood-specific RNAi approach was sufficient to induce excessive higher-order branches at Day 3 (Fig. 3H-K). This effect was confirmed using an additional RNAi clone we constructed to target a different coding region for each gene (Fig. S4M-P).

Importantly, we found that Day 3 *col-120 (sy1526)* mutants exhibited a significant decrease in both mean wavelength and mean amplitude of their sinusoidal movement, remarkably similar to that observed in control Day 9 animals, albeit without affecting the variability in these parameters (Fig. 3L-N, Fig. S4Q-R). Collectively, we demonstrated that skin collagens, DPY-5 and COL-120, play a critical role in regulating the integrity of PVD dendritic branching and PVD-navigated proprioceptive function, particularly in aging. Given the improbable physical interaction between these apically secreted cuticular collagens and PVD dendritic structures, our findings suggest that age-related decrease in skin collagens actively contributes to the aging of cutaneous sensory neurons independently of their traditionally recognized role in providing direct structural support for neurons.

2.4 Overexpression of skin collagen genes delays the onset of aging-associated excessive PVD dendritic branching

We further examined the impacts of overexpressing *dpy-5* or *col-120* in control animals to solidify their aging-associated roles in maintaining PVD dendritic branching integrity. Using the *col-19* promoter (Thein et al., 2003) we induced the overexpression of *dpy-5* in the epidermis

specifically during adulthood. Our data indicate that adulthood-specific overexpression of *dpy-5* effectively mitigated excessive dendritic branches when examined at Day 9 of adulthood (Fig. 4A-B). Similar positive effects were also observed with ubiquitous overexpression of *col-120* (Fig. 4C-D; additional overexpression line in Fig. S5A-B). Moreover, epidermal overexpression of *dpy-5* appeared to shift proprioceptive function parameters in Day 9 animals towards those of a younger age, as evidenced by a trend towards increased mean wavelength and amplitude in their movement tracks, though this did not reach statistical significance (Fig. S5D-G). It is important to acknowledge that age-related declines in other systems, such as muscles and motor neurons, may complicate the assessment of the sensory aspect of proprioception at this stage of life. Interestingly, using the same overexpression strategy, we found that neither *dpy-5* nor *col-120* significantly affected lifespan (Fig. 4E, Fig. S5C). While previous studies have reported a slight lifespan extension with *col-120* overexpression (Ewald et al., 2015), discrepancies with our results may be attributed to differences in the promoters and 3'UTR sequences used to construct transgenic strains. Nevertheless, our findings suggest that the observed aging-associated neuroprotective effects of skin collagen are distinctly targeted towards neuronal integrity, rather than through promoting longevity.

2.5 DPY-5 and COL-120 are not involved in aging-associated dendritic beading in PVD neurons

To investigate whether skin collagen genes regulate the overall aging of PVD neurons, we examined the effects of *dpy-5* or *col*-120 mutation on the previously documented aging-associated dendritic beading phenotype (Fig. S1A) (E et al., 2018; Saberi-Bosari et al., 2020). Notably, the extent of PVD dendritic beading in Day 3 *dpy-5 (e907)* or *col-120 (sy1526)* mutant animals was comparable to that observed in age-matched controls (Fig. 5A). Coupled with our observations of a potential inverse relationship between aging-associated dendritic beading and excessive dendritic branching in older control animals (Fig. S3V-W), these results suggest that *dpy-5* and *col-120* regulate PVD dendritic structure via mechanisms separate from those leading to the dendritic beading degenerative phenotype, such as the skin antimicrobial peptide NLP-29 (E et al., 2018). This is also supported by previous research showing that mutations in *dpy-5* and *col-120* do not impact *nlp-29* expression (Dodd et al., 2018; Zhu et al., 2023). Collectively, our findings support the notion that distinct non-neural molecular

327 mechanisms may be underlying different dimensions of neuronal aging, even within an
328 individual neuron.

329 **2.6 ALM sensory neurons exhibit ectopic branching in response to *dpy-5* loss-of-**
330 **function mutation, but PLM neurons do not**

331 To determine whether the regulatory role of skin collagens in neuron structural integrity is
332 specific to certain neuron sub-types we examined the effects of *dpy-5* mutation on two
333 additional sub-types of cutaneous sensory neurons in *C. elegans*: the ALM and PLM touch
334 receptor neurons, which are crucial for the perception of gentle touch (Corsi et al., 2015).
335 Intriguingly, Day 3 *dpy-5 (e907)* mutant animals exhibited an increase in ectopic, aberrant
336 branching from ALM anterior neurites when compared to Day 3 control animals, while PLM
337 neurons showed no morphological abnormalities (Fig. 5B-D). This discrepancy indicates that
338 the regulatory role of skin collagens in neuritic branching may not extend uniformly across all
339 cutaneous sensory neurons, suggesting that certain neuron sub-types may possess unique
340 features rendering them particularly vulnerable to the effects of skin collagen loss during aging.

341 **2.7 RIG-3/IgSF functions along with skin collagens to regulate aging-associated**
342 **excessive PVD dendritic branching**

343 We next explored the potential mechanism by which skin collagen genes regulate PVD
344 dendritic branching during aging. In the developing nervous system, a variety of
345 transmembrane and extracellular proteins are crucial for facilitating adhesive interactions that
346 are critical to neuronal shape remodeling and migration (Hobert, 2013; Rozario & DeSimone,
347 2010). Proteins such as SAX-7/L1CAM, MNR-1, DMA-1 (transmembrane LRR protein), and
348 UNC-52/perlecan have been extensively studied in relation to PVD dendritic morphogenesis
349 (Dong et al., 2013; Salzberg et al., 2013). Yet, it is unlikely that these elements contribute to
350 the aging-associated increase in PVD higher-order dendritic branching. This is because
351 epidermally-expressed SAX-7 primarily guides the outgrowths of 1°- 4° dendritic branches, and
352 evidence shows that SAX-7's epidermal localization aligns with 1°- 4° dendrites but not with
353 higher-order branches (Liang et al., 2015; Ramirez-Suarez et al., 2019). Similarly, DMA-1
354 overexpression only induces aberrant dendritic branching at 3° level (Dong et al., 2013; Liu &

355 Shen, 2011). We therefore hypothesized that different cell adhesion molecules might play a
356 role in aging-associated excessive branching due to loss of skin collagens.

357 Through a targeted RNAi screen specifically in adulthood, we found that knockdown of *ina-1*
358 (which codes for an integrin alpha-subunit) or *rig-3* (which codes for a protein of the
359 Immunoglobulin Superfamily/IgSF) led to early-onset excessive dendritic branching in PVD
360 neurons (Fig. 6A-B, Fig. S6A-B). Unlike the widespread expression of *ina-1* in various tissues,
361 *rig-3* is distinctly expressed in select neurons including AVA interneurons but is notably not
362 detectable in PVD neurons or in the epidermis (Babu et al., 2011; Oliver et al., 2019; Taylor et
363 al., 2021). Therefore, RIG-3 emerges as a compelling candidate for further investigation into its
364 potential non-cell-autonomous role in PVD dendritic branching. Our analysis of *rig-3(ok2156)*
365 loss-of-function mutant animals confirmed our initial findings from RNAi experiments and also
366 demonstrated that *rig-3* does not impact PVD dendritic morphogenesis during development
367 (Fig. S6C-F). To investigate the role of *rig-3* in the regulation of PVD excessive branching by
368 skin collagens, we performed adulthood RNAi knockdown of *rig-3* in *col-120* or *dpy-5* mutant
369 animals. Remarkably, *rig-3* RNAi-treated *dpy-5(e907)* or *col-120(sy1526)* mutant animals did
370 not exhibit further excessive branching when compared to empty vector-treated mutants,
371 suggesting that *rig-3* functions in the same genetic pathway as *dpy-5* or *col-120* in regulating
372 PVD dendritic integrity during aging (Fig. 6C-D).

373 In a complementary approach to further explore the downstream mechanisms of skin collagen
374 genes, we analyzed publicly available microarray data (GEO accession GSE19310) comparing
375 N2/WT and *dpy-10(e128)* mutant animals at the young adult stage (Rohlfing et al., 2010). *dpy-*
376 *10* is another cuticular collagen gene downregulated with age (Fig. S4A). Notably, *dpy-*
377 *10(e128)* mutants also exhibit early-onset excessive dendritic branching in PVD neurons (Fig.
378 S6G-H), similar to *dpy-5* and *col-120* mutant animals. Intriguingly, KEGG pathway analysis of
379 the differentially expressed genes from the datasets (GSE19310) revealed that the Wnt
380 signaling pathway was among the top downregulated pathways in *dpy-10(e128)* animals
381 compared to WT animals (Fig. S6I). Wnt signaling is known to play a crucial role in guiding
382 dendritic morphogenesis during development, controlling branch point selection, and limiting
383 dendritic expansion into non-permissive territories (Lanoue & Cooper, 2019), though its
384 specific involvement in the PVD phenotype studied here remains unknown. Previous studies

have shown that extracellular RIG-3 restricts neuronal polarity during development by interacting with a Wnt receptor in a non-cell-autonomous manner (Babu et al., 2011; Pandey et al., 2017). Given the absence of *rig-3* expression in the epidermis or PVD neurons (Schwarz et al., 2009; Taylor et al., 2021), it is plausible to speculate that RIG-3 may operate from adjacent neurons, such as AVA interneurons (Smith et al., 2010; Way & Chalfie, 1989; White et al., 1986), to relay signals from skin collagens and regulate PVD dendritic branching possibly through Wnt signaling. Future investigations are necessary to elucidate the precise recruitment and signaling hierarchy of these events. Our findings collectively demonstrate the crucial role of skin collagen reduction in driving selective aspects of aging-associated decline in sensory neuron integrity, potentially mediated through a series of cellular communication processes involving cell adhesion molecules with signaling functions.

3. DISCUSSION

In this study we have identified a novel role for skin collagens in regulating the aging of cutaneous sensory neurons, using *C. elegans* PVD neurons as a model. Specifically, we demonstrate that loss of function mutations in non-basement membrane collagens, namely *dpy-5* or *col-120*, lead to an early-onset of aging-associated excessive dendritic branching in PVD neurons. Moreover, we further confirm the neuroprotective capacity of overexpressing these skin collagen genes in aged animals. In-depth analysis reveals that the excessive PVD dendritic branching associated with aging is strongly and distinctly correlated with proprioceptive deficits typically observed during normal aging. Notably, young adult animals with a *col-120* loss of function mutation exhibit proprioceptive deficits similar to those in aged wild-type animals, further indicating the critical regulatory role skin collagens play in both morphological and functional aging of sensory neurons. Our results also emphasize the selective impact of skin collagens on the aging of sensory neurons. This selectivity is evident at two distinct levels: firstly, skin collagens appear not to contribute to the development of neuritic beading in aging PVD neurons, pointing to a phenotype-specific effect; secondly, their role is confined to regulating the branching integrity of specific sub-types of cutaneous sensory neurons, highlighting a targeted cell-cell communication. Additionally, we identify that the neural cell adhesion protein RIG-3/IgSF, which is not expressed in PVD neurons or the skin, acts as a partner with skin collagens in preserving dendritic integrity in PVD neurons during

415 aging. Taken together, our findings suggest that the regulatory role of skin collagens is
416 mediated through intricate cellular communication processes rather than by directly providing
417 structural support for neurons. Our study further highlights the possibility that various molecular
418 cues from non-neural tissues during aging may activate distinct mechanisms, inducing specific
419 morphological changes in neurons that lead to unique functional consequences. This
420 underscores the need for a paradigm shift towards exploring multi-tissue strategies to
421 comprehensively address the complexities of neuronal aging.

422 While age-related declines in collagen production in various tissues have been well-
423 documented (Fatima et al., 2022; Kehlet et al., 2018; Stammers et al., 2020; Varani et al.,
424 2006), research investigating their potential impact on the nervous system during aging is
425 scarce. A study reported that aged mice lacking COL6A1, a ubiquitously expressed collagen VI
426 gene, exhibited more severe deficits in motor coordination and spatial memory compared to
427 age-matched WT animals (Cescon et al., 2016). Our current study further expands this
428 research area by demonstrating that non-basement membrane collagens, particularly those
429 from non-neural tissues, play a distinctive regulatory role in the structural and functional
430 integrity of neurons during aging. However, the precise molecular mechanisms underlying the
431 collagen's non-cell-autonomous effects will require clarification. Our previous research has
432 revealed that the epidermally-expressed antimicrobial peptide, NLP-29, triggers aging-
433 associated dendritic beading in *C.* elegans PVD neurons through its interaction with a
434 neuropeptide receptor, NPR-12, which then activates an autophagy-mediated
435 neurodegeneration signal (E et al., 2018). Similarly, studies in mice show that neurotrophin 3
436 (NT3), which is downregulated in aging skin, can affect cutaneous nerve innervations during
437 aging, possibly due to diminished signaling between NT3 and its neuronal receptor, trkA
438 (Bergman et al., 2000). While it is unlikely for the cuticular collagens we studied here to directly
439 interact with sensory endings, literature evidence points to a possibility that receptors or cell-
440 surface molecules on sensory neurons may indirectly receive cues from age-related reduction
441 in skin collagens.

442 Cell-adhesion molecules (CAMs) play a pivotal role in the spatial development of the nervous
443 system across various organisms (Hobert, 2013; Rozario & DeSimone, 2010). However, as
444 discussed above, CAMs required for PVD dendritic morphogenesis, including SAX-7 and

445 DMA-1 (Dong et al., 2013; Liang et al., 2015; Salzberg et al., 2013), do not seem to be
446 involved in the aging process of PVD neurons. Our study identifies neuronal RIG-3/IgSF as a
447 collaborator with skin collagens in modulating dendritic branching specifically during adulthood,
448 suggesting that specific CAMs may be distinctively involved in neural development and neural
449 aging. RIG-3 shares sequence homology with mammalian neural cell adhesion molecule 1
450 (NCAM1), also an IgSF protein (Babu et al., 2011). Studies in a rat sciatic nerve injury model
451 have shown that NCAM1 on the axonal membrane is necessary for proper axonal fasciculation
452 during nerve regeneration, requiring the physical interaction between extracellular collagen VI
453 and the fibronectin type III (FNIII) domain of NCAM1 (Sun et al., 2022). While RIG-3 also
454 contains a FNIII domain (Babu et al., 2011), whether it directly interacts with COL-120 or DPY-
455 5 remains to be determined. Intriguingly, based on the distinct neuronal expression pattern of
456 *rig-3* in wild-type animals (Babu et al., 2011; Oliver et al., 2019; Taylor et al., 2021), RIG-3 may
457 not directly function on the surface of the PVD neurons to receive cues from skin collagens,
458 but potentially from nearby neurons, such as AVA or PVC interneurons, which the PVD neuron
459 synapses onto (Bhardwaj et al., 2020). This points to an intricate model involving multiple
460 layers of intercellular communication for the bridging mechanisms between skin collagens and
461 sensory neuron health in aging.

462 Excessive branching in peripheral neurons triggered by aging is a conserved phenomenon.
463 Studies on rats aged between 25 to 28 months demonstrate an abrupt increase in the motor
464 neuron terminal branches at the diaphragm and leg muscles, with this increase diminishing at
465 later ages (Rosenheimer & Smith, 1985). Similarly, older humans with sensory neuropathy
466 exhibit increased epidermal nerve fiber branching at the proximal thigh compared to healthy
467 controls (Lauria et al., 1999). Our time-lapse imaging revealed that excessive high-order
468 dendritic branches in PVD neurons are enriched with F-actin and lack microtubules, indicating
469 high dynamic potential. This cytoskeletal makeup and dynamic behavior resemble dendritic
470 spines (Cuentas-Condori et al., 2019), alterations in which can impact neuronal activity or
471 synaptic plasticity (Kasai et al., 2003; Lippman & Dunaevsky, 2005). It is tempting to speculate
472 that increased branching observed in aging reflects a compensatory plasticity for future
473 neurodegeneration at more advanced ages. However, this speculation relies on understanding
474 the functional significance of these excessive branches, especially considering that PVD
475 dendrites are not known to form synapses with other neurons.

Our findings indicate that excessive higher-order branches in aging PVD neurons are functionally relevant to proprioceptive deficits observed during normal aging. Proper proprioception in young healthy *C. elegans*, particularly in the form of their sinusoidal movements, involves a mechanosensitive sodium channel (MEC-10, UNC-8, and DEL-1) in lower-order dendritic branches of PVD (Tao et al., 2019). Upon proprioceptive stimuli, this channel is activated to induce local Ca^{2+} increase and dendritic release of the neuropeptide NLP-12, which directly modulates the neuromuscular junctions to regulate movement vigor (Tao et al., 2019). Further investigation is necessary to determine whether the sodium channel distribution or the neuropeptide release patterns change with age, potentially contributing to age-related proprioceptive deficits relevant to excessive PVD dendritic branching. Such investigations may also provide insights into whether aging-associated excessive branching in the peripheral nervous system represents aberrant compensatory plasticity that inappropriately engages sensorimotor networks.

We show that a polymodal sensory neuron can develop multiple distinct morphological changes during aging, each corresponding to a decline in specific neuronal functions. In PVD neurons, simultaneous excessive dendritic branching and dendritic beading are rare in normal aging, making it unlikely for an animal to experience a significant decline in both harsh touch function and proprioception concurrently. The question of whether polymodal neurons prioritize one function over another remains unanswered. Nevertheless, our previous research (E et al., 2018) and current study together provide intriguing evidence suggesting that within the same multifunctional neuron, there is selectivity regarding which structure and function are more vulnerable to aging, likely mediated by distinct non-neural signals.

On a broader scale, neurons in different regions of the nervous system also exhibit varying susceptibility or resistance to aging, leading to differences in the onset timing and progression of neurodegenerative processes. This phenomenon, known as selective neuron vulnerability, is commonly observed in both normal aging and age-related neurodegenerative diseases (Feng et al., 2020; Saxena & Caroni, 2011), though the underlying basis of this selectivity remains elusive. Importantly, this phenomenon is evolutionarily conserved, also observed in *C. elegans* ALM, PLM, and PVD neurons (E et al., 2018; Pan et al., 2011; Toth et al., 2012), which were the focus of our study. These neurons not only begin aging at different times and rates but also

respond differently to the same skin-derived molecular cue, as demonstrated in our study. Given that each neuron class/sub-type has a distinct gene expression pattern (Huntley et al., 2020; Taylor et al., 2021; Wallace et al., 2020), future research is needed to investigate whether the unique cell surface molecular signatures of each subset of neurons dictate which non-neural or extracellular aging signals they receive, thus creating the selective vulnerability.

ACKNOWLEDGMENTS

We thank Bradey A. R. Stuart and Swapnil G. Waghmare for assistance in molecular cloning and construction of transgenic strains. Some strains were provided by the CGC, which is funded by NIH Office of Research Infrastructure Programs (P40 OD010440).

CONFLICT OF INTEREST

The authors declare that the research was conducted in the absence of any commercial or financial relationships that could be construed as a potential conflict of interest.

FUNDING SUPPORT

This work was supported by the Imagine More Award and Research Affairs Committee at the Medical College of Wisconsin, as well as Advancing a Healthier Wisconsin (AHW) Endowment project 5520482 titled Developing Innovative Translational Research Programs in Clinically Relevant Neurological Disorders.

AUTHOR CONTRIBUTIONS

L.E. conceived the project; L.E. and M.K. designed the experiments; M.K., A.L.F., and L.E. performed the experiments and collected the data; M.K. and L.E. analyzed and interpreted the data; M.K. and L.E. drafted the manuscript; M.K., A.L.F. and L.E. edited and proofread the manuscript.

DATA AVAILABILITY

The data that support the findings of this study are available from the corresponding author upon reasonable request.

FIGURE LEGENDS

Figure 1: Aging triggers the progressive development of excessive higher-order dendritic branching in PVD neurons

(A) Schematic diagram of PVD neuron in control (CT) animals [*F49H12.4::GFP (wdIs51)*]. Black boxes indicate regions imaged.

(B) A 'menorah' structure with orders of dendritic branching indicated.

(C) Representative images of anterior (Zone 1) and posterior (Zone 2) sections of PVD neuron at Day 1 (D1) and D9 of adulthood in CT animals. Blue boxes indicate zoomed in section for Zone 1, Red boxes indicate zoomed in section for Zone 2. Yellow arrowheads indicate PVD soma, and blue arrowheads indicate PVD axon. White arrowheads indicate 5º dendritic branches and red arrowheads indicate 6º dendrites. Scale bar = 20 μm. Mild autofluorescence of gut granules, a normal physiological feature in *C. elegans*, appears as small punctate structures in the background.

(D-E) Quantification of 5º *(D)* and 6º *(E)* dendrites during aging in CT animals. *n* >50 per group.

(F-G) Quantification 5º *(F)* and 6º *(G)* dendrites in CT animals at 15 ºC, 20 ºC, and 25 ºC. *n* >36/group.

(H-I) Quantification of dorsal 6º dendrites normalized to the number of dorsal menorah *(H)* and ventral 6º dendrites normalized to the number of ventral menorah *(I)*. *n* >10/group.

(J-K) Quantification of dorsal 6º dendrites normalized to dorsal 4º dendrites *(J)* and ventral 6º dendrites normalized to ventral 4º dendrites *(K)*. *n* >10/group.

(L-M) Quantification of anterior 6º dendrites normalized to the number of anterior menorah *(L)* and posterior 6º dendrites normalized to the number of posterior menorah *(M)*. *n* >25/group.

(N-O) Quantification of anterior 6º dendrites normalized to anterior 4º dendrites *(N)* and posterior 6º dendrites normalized to posterior 4º dendrites *(O)*. *n* >25/group.

(P) Representative time-lapse images of actin dynamics in higher-order dendritic branches during an 8-minute session at 2-minute intervals in D1 and D9 CT animals [*ser-2(3)p::GFP::UtrCH + ser-2(3)p::mCherry-PH(lxyEx51)*]. mCherry::PH/membrane-bound mCherry was used to visualize PVD structure. Yellow arrows indicate 2º and 3º dendrites.

559 White arrowheads indicate 5º dendrites and red arrowheads indicate 6º dendrites, with
560 asterisks indicating dendrites where a dynamic actin remodeling event occurs. Scale bar = 10
561 μm.

562 **(Q-R)** Changes in the length of higher-order dendrites relative to their initial lengths were
563 tracked using time-lapse imaging data obtained from D1*(Q)* and D9 *(R)* CT animals as in *(P).*
564 Measurements were taken for 5º and 6º dendrites branching from 4º and 5º dendrites,
565 respectively, with each line representing a single higher-order dendrite. *n* (animals imaged) =
566 3/group. **(S)** Absolute change in branch length over 8 minutes in D1 and D9 CT animals, with
567 each point representing a higher-order dendrite. *n* (animals imaged) = 3/group.

568 * $p<0.05$, ** $p<0.005$, *** $p<0.001$, **** $p<0.0001$.

569

570 **Figure 2: Aging-associated excessive dendritic branching in PVD neurons correlates**
571 **with proprioceptive deficits**

572 **(A)** Representative images of movement tracks of control (CT) animal at Day 3 (D3) and D9 of
573 adulthood. Scale bar = 50 μm.

574 **(B-C)** Mean amplitude *(B)* and mean wavelength *(C)* measured from 100 tracks per animal in
575 CT animals. Normalized for animal body length. *n* >28 per group.

576 **(D-E)** Variability in amplitude *(D)* and wavelength *(E)* measured via coefficient of variability
577 (CV) from 100 tracks per animal in CT animals. *n* >28/ group.

578 **(F-I)** Correlation between proprioception measurements and number of PVD dorsal 6º dendritic
579 branches. *n* >28/group.

580 * $p<0.05$, *** $p<0.001$, **** $p<0.0001$.

581

582 **Figure 3: Loss of skin collagen leads to early-onset of aging-associated excessive**
583 **branching and proprioceptive deficit**

584 **(A)** Domain structures of COL-120 and DPY-5, with key features annotated. Adapted from
585 CeCoIDB (Teuscher et al., 2019).

586 **(B-C)** Representative images of excessive PVD dendritic branching in *dpy-5* mutant [*dpy-*
587 *5(e907); F49H12.4::GFP(wdIs51)*] *(B)* and *col-120* mutant (*col-120(sy1526); F49H12.4::GFP*
588 *(wdIs51)*) *(C)* at Day 3 (D3) of adulthood. White arrowheads indicate 5º dendrites, and red
589 arrowheads indicate 6º dendrites. Scale bar = 50 μm.

590 **(D-E)** Quantification of 5º *(D)* and 6º *(E)* dendrites in CT, *dpy-5(e907)* mutant, and *dpy-5* rescue
591 line 1 (epidermis-specific rescue driven by *dpy-7* promoter) animals. *n* >60 per group.

592 **(F-G)** Quantification of 5º *(F)* and 6º *(G)* dendrites in CT, *col-120(sy1526)* mutant, and *col-120*
593 rescue line 1 (epidermis-specific rescue driven by *dpy-7* promoter and *col-19* promoter)
594 animals. *n* >55/group.

595 **(H-I)** Quantification of 5º *(H)* and 6º *(I)* dendrites in empty vector (EV) and *dpy-5* RNAi treated
596 animals. *n* >70/group.

597 **(J-K)** Quantification of 5º *(J)* and 6º *(K)* dendrites in EV and *col-120* RNAi treated animals. *n*
598 >70/group.

599 **(L)** Representative images of movement tracks of D3 CT, D9 CT and D3 *col-120(sy1526)*
600 mutant animals. Scale bar = 50 μM.

601 **(M-N)** Mean wavelength *(M)* and mean amplitude *(N)* measured from 100 tracks per animal for
602 D3 CT, D9 CT, and D3 *col-120(sy1526)* mutant animals. Normalized for animal body length. *n*
603 >28/group. ns-not significant,

604 * $p<0.05$, ** $p<0.005$, *** $p<0.001$, **** $p<0.0001$.

605

606 **Figure 4: Overexpression of skin collagen mitigates aging-associated excessive**
607 **dendritic branching in PVD neurons**

608 **(A-B)** Quantification of 5º *(A)* and 6º *(B)* dendrites in control (CT) and *dpy-5* overexpression
609 (epidermis-specific overexpression driven by *col-19* promoter) animals at Day 9 (D9) of
610 adulthood. *n* >46 per group.

611 **(C-D)** Quantification of 5º *(C)* and 6º *(D)* dendrites in CT and *col-120* overexpression
612 (ubiquitous overexpression driven by *dpy-30* promoter) animals. *n* >63 per group.

613 **(E)** Lifespan analysis of CT, *dpy-5* overexpression and *col-120* overexpression animals. No
614 statistical significance was detected compared to CT. *n* >12 for each group.

615 * *p*<0.05, ** *p*<0.005, *** *p*<0.001.

616

617 **Figure 5: Selective impact of skin collagens on the aging process of sensory neurons**

618 **(A)** Quantification of PVD dendritic beading in control (CT), *dpy-5(e907)* mutant, and *col-*
619 *120(sy1526)* mutant animals at Day 3 (D3) of adulthood. Scored based on severity of beading
620 phenotype. *N* >26 per group.

621 **(B)** Schematic diagram of ALM and PLM neuron, with a representative image of the ALM
622 neuron in CT [*mec-4p::GFP(zdIs5)*] and *dpy-5* mutant [*dpy-5(e907); mec-4p::GFP (zdIs51)*]
623 animals at D3 of adulthood. Scale bar = 50 μm. White arrowhead indicates ectopic branching
624 from ALM anterior neurite; yellow arrowheads indicate ALM soma.

625 **(C-D)** Quantification of ectopic branches in ALM *(C)* and PLM neuron *(D)* in CT and *dpy-*
626 *5(e907)* mutant animals at D3. Number of ectopic branches observed per animal is indicated. *n*
627 >78 per group.

628 **** *p*<0.0001.

629

630 **Figure 6: RIG-3/IgSF functions along with skin collagens to regulate aging-associated**
631 **excessive PVD dendritic branching**

632 **(A-B**) Quantification of 5º *(A)* and 6º *(B)* dendrites in empty vector (EV) and *rig-3* RNAi treated
633 control animals (*F49H12.4::GFP (wdIs51)*) . *n*>84/group.

634 **(C-D)** Quantification of 5º *(C)* and 6º *(D)* dendrites in *dpy-5(e907)* mutant animals treated with
635 EV or *rig-3* RNAi, as well as in *col-120(sy1526)* mutant animals treated with EV or *rig-3* RNAi.
636 *n* >84/group.

637 * *p*<0.05, *** *p*<0.001, **** *p*<0.0001.

638

SUPPORTING INFORMATION

Figure S1: Characterization of the aging PVD neuron
(A) Schematic diagram of the PVD neuron in control (CT) animals. The black box indicates the zone presented in the representative image of CT animals at Day 11 (D11) of adulthood. Yellow arrowheads indicate neuritic beads. Scale bar = 50 μm. **(B**) Correlation between PVD beading severity and harsh touch response in CT [*mec-4(u253)*; *F49H12.4::GFP(wdIs51)*] animals at D7. See Methods for scoring criteria. *n*>20 . (**C-F)** Quantification of the number of dorsal 5º dendrites *(C)*, ventral 5º dendrites *(D)*, dorsal 6º dendrites *(E)*, and ventral 6º dendrites *(F)* in CT [*F49H12.4::GFP(wdIs51)*] animals, *n* >54/group. **(G-J)** Quantification of number of dorsal *(G)*, ventral *(H)*, anterior *(I)*, and posterior *(J)* menorah. *n* >10/group. **(K-N)** Quantification of number of dorsal *(K)*, ventral *(L)*, anterior *(M)*, and posterior *(N)* 4º dendrites. *n* >10/group. **(O-P)** Quantification of number of dorsal *(O)* and ventral *(P)* 5º dendrites normalized to number of menorahs. *n* >10/group. **(Q-R)** Quantification of number of dorsal *(Q)* and ventral *(R)* 5º dendrites normalized to number of 4º dendrites. *n* >10/group. **(S-T)** Quantification of number of anterior *(S)* and posterior *(T)* 5º dendrites normalized to number of menorahs. *n* >10/group. **(U-V)** Quantification of number of anterior *(U)* and posterior *(V)* 5º dendrites normalized to number of 4º dendrites. *n* >10/group. **(W-X)** Quantification of number of 5º *(W)* and 6º *(X)* dendrites normalized to body length. *n* >28 per group. * $p<0.05$, ** $p<0.005$, *** $p<0.001$, **** $p<0.0001$.

Figure S2: Actin and microtubule dynamics in the PVD neuron
(A) Split channel and merged images of microtubule localization in the PVD neuron at Day 7 (D7) in control (CT) animals [*ser-2(3)p::EMTB::GFP* + *ser-2(3)p::mCherry-PH(lxyEx48)*]. Red channel displays the PVD neuron, while the green channel displays the microtubules in the PVD. **(B)** Split channel representative time-lapse images of actin dynamics in higher order dendrites during an 8 minute session at 2 minute intervals at D1 and D9 of adulthood in CT animals [*ser-2(3)p::GFP::UtrCH* + *ser-2(3)p::mCherry-PH(lxyEx51)*]. Red channel displays the PVD neuron, while the green channel displays the actin in the PVD. Scale bar = 10 μm.

Figure S3: Aging-associated dendritic branching correlated with proprioceptive deficits and neuritic beading
(A) Correlation between number of higher-order dendrites (5º and 6º) and harsh touch response in *mec-4* mutant animals at Day 7 (D7) of adulthood. Harsh touch response was scored based on the distance moved with a cumulative score ranging from 0 to 10, indicating impaired to normal response respectively. **(B-C)** Correlation between variability in amplitude (CV) and higher-order dendrites in control (CT) animals at D3 and D9 of adulthood. Higher-order dendrites are 5º dendrites *(B)* and 6º dendrites *(C)*. *n* >28 for each group. **(D-E)** Correlation between wavelength CV and higher-order dendrites in CT animals at D3 and D9. Higher-order dendrites are 5º dendrites *(D)* and 6º dendrites *(E)*. *n* >28 for each group. **(F-G)** Correlation between mean amplitude and higher-order dendrites in CT animals at D3 and D9. Higher-order branches are 5º dendrites *(F)* and 6º dendrites *(G)*. *n* >28 for each group. **(H-I)**

Correlation between mean wavelength and higher-order branches in CT animals at D3 and D9. Higher-order dendrites are 5º dendrites *(H)* and 6º dendrites *(I)*. *n* >28 for each group. **(J-U)** Either dorsal or ventral dendrites were measured for individual animals. Only animals whose dorsal dendrites were measured were used for analysis of dorsal branch correlation, and the same for ventral dendrite analysis. **(J-M)** Correlation between proprioception measurements and number of ventral 6º dendrites at D3 and D9 in CT animals. Proprioceptive measurements are amplitude CV *(J)*, wavelength CV *(K)*, mean amplitude *(L)*, and mean wavelength *(M)*. *n* >28/group. **(N- Q)** Correlation between proprioception measurements and number of dorsal 5º dendrites at D3 and D9 in CT animals. Proprioceptive measurements are Amplitude CV *(N)*, wavelength CV *(O)*, mean amplitude *(P)*, and mean wavelength *(Q)*. *n* >28/group. **(R- U)** Correlation between proprioception measurements and number of ventral 5º dendrites at Days 3 and 9 in CT animals. Proprioceptive measurements are amplitude CV *(R)*, wavelength CV *(S)*, mean amplitude *(T)*, and mean wavelength *(U)*. *n* >28/group. **(V-W)** Correlation between higher-order branching and the extent of neuritic beading in CT animals at D8 (circles) and D9 (triangles) of adulthood. Higher-order dendrites are 5º dendrites *(V)* and 6º dendrites *(W)*. Beading severity is measured as 0- normal ,1- mild, 2- moderate, and 3 -severe. *n* >11/group.

Figure S4: Characterization of loss of skin collagens

(A) (Left) Volcano plot depicting changes in expression of skin collagens in Day 10 (D10) animals relative to L4 animals from the GSE176088 dataset (Sheng & Xiao, 2021). *col-120, dpy-5,* and *dpy-10* are shown in orange. (Right) qPCR verification of *dpy-5* and *col-120* mRNA expression levels in control (CT) animals at D1 and D7, represented as relative quantity, with *ama-1* as the housekeeping gene. **(B)** *dpy-5* and *col-120* mRNA expression levels after adulthood-specific RNAi treatment relative to empty vector (EV) control, represented as relative quantity z-score, with *ama-1* as the housekeeping gene. **(C)** Comparison of body lengths between control (CT) and *col-120* mutant animals at D3. *n* >25 per group. **(D)** Lifespan analysis of CT, *dpy-5* mutant and *col-120* mutant animals. *n* >16/group. **(E-F)** Quantification of 5º *(E)* and 6º *(F)* dendrites in CT, *dpy-5* mutant, and *dpy-5* rescue line 2 (Epidermis-specific rescue driven by *dpy7(SI)* promoter) animals at D3. *n* >20/group. **(G-H)** Quantification of 5º *(G)* and 6º *(H)* dendrites in CT, *col-120* mutant, and *col-120* rescue line 2 (Epidermis-specific rescue driven by *col19* promoter) animals at Day 3. *n* >81/group. **(I-J)** Quantification of 5º *(I)* and 6º *(J)* dendrites in CT, *dpy-5* mutant, and *col-120* mutant animals at L4 stage. *n* >20/group. **(K-L)** Quantification of 5º *(K)* and 6º *(L)* dendrites in empty vector (EV) animals at D3 and D9. *n*> 30/group. **(M-N)** Quantification of 5º *(M)* and 6º *(N)* dendrites in EV and *dpy-5* RNAi clone 2 at D3. *n* >23/group. **(O-P)** Quantification of 5º *(O)* and 6º *(P)* dendrites EV and *col-120* RNAi clone 2 at D3. *n* >30/group. **(Q-R)** Quantification of wavelength CV *(Q)* and amplitude CV *(R)* in CT Day 3, CT Day 9, and *col-120* mutant animals at D3. *n* >25/group. * $p<0.05$, ** $p<0.005$, *** $p<0.001$, **** $p<0.0001$.

Figure S5: Overexpression of skin collagens does not delay onset of proprioceptive deficit

(A-B) Quantification of 5º *(A)* and 6º *(B)* dendrites in control (CT) and *col-120* overexpression line 2 (ubiquitous overexpression driven by *dpy30* promoter) animals at Day 9 (D9) of adulthood. *n* >20 for each group. **(C)** Additional replicate of lifespan analysis of CT, and *col-120* overexpression animals. *n* > 23/group. **(D-G)** Quantification of mean wavelength normalized to control *(D)*, mean amplitude normalized to control *(E)*, wavelength CV *(F)*, and amplitude CV *(G)* in CT and *dpy-5* epidermis-specific overexpression (driven by *col-19* promoter) animals. *n* >21/ group. ** *p*<0.005.

Figure S6: Additional mediators of excessive dendritic branching
(A-B) Quantification of 5º *(A)* and 6º *(B)* dendrites in empty vector (EV), *ina-1* RNAi, *ddr-2* RNAi, *sdn-1* RNAi treatment at Day 3 (D3) of adulthood. *n* >30 per group. **(C-D)** Quantification of 5º *(C)* and 6º *(D)* dendrites in control (CT, *ser-2(3)p::GFP (lxyEx77)*, see Methods) and *rig-3* mutant [*rig-3(ok2156); ser-2(3)p::GFP (lxyEx77)*] animals at D1. *n* >86/group. **(E-F)** Quantification of 5º *(E)* and 6º *(F)* dendrites in control (CT, *ser-2(3)p::GFP (lxyEx77)*, see Methods) and *rig-3* mutant [*rig-3(ok2156); ser-2(3)p::GFP (lxyEx77)*] animals at L4. *n* >10/group. **(G-H)** Quantification of 5º *(G)* and 6º *(H)* dendrites in control (CT, *F49H12.4::GFP(wdIs51)*) and *dpy-10* mutant (*dpy-10(e128); F49H12.4::GFP(wdIs51)*) animals. *n* = 50/group. **(I)** KEGG pathway analysis between control and *dpy-10 (e128)* mutant animals, using the publicly available microarray dataset (GSE19310) (Rohlfing et al., 2010). ** *p*<0.005, **** *p*<0.0001.

Table S1: Comparison of branching in PVDL and PVDR neurons
Difference between medians for WT animals at Day 3, 6, 9 for Right and Left PVD neurons' 5º and 6º dendrites. *n* >19 per group.

METHODS

C. elegans Strains and Maintenance

C. elegans strains were maintained at 20 °C, or as otherwise indicated, on Nematode Growth Medium (NGM) plates seeded with *E. coli* OP50 as described previously (Brenner, 1974). Only hermaphrodites were utilized for data generating experiments. Males were utilized for genetic crosses alone. For aging-related experiments, plates containing gravid hermaphrodites were bleached to produce age-synchronous progeny and to eliminate potential pathogenic microbes. Once the animals reached mid-L4 or late-L4 stage, they were transferred to NGM plates containing 100 μM 5' fluorodeoxyuridine (FUDR) (VWR, 76345-984) to prevent egg hatching and to maintain age-synchronous population (Glenn et al., 2004; Wang et al., 2019). Day 1 of adulthood was defined as occurring 24 hours after the L4 stage. For strain information, see Table S2.

DNA Constructs and Generation of Transgenes

Gateway cloning technology (ThermoFisher, K250020, 11791020) was used to create all DNA expression constructs, and information about the individual constructs is listed in Table S3. Primers were acquired from Millipore and ThermoFisher, and details are included in Table S4. The transgenic animals were generated using the standard procedures through microinjection (Berkowitz et al., 2008). In general, plasmid DNAs of interest were used at 10-100 ng/μL with the co-injection marker *ttx-3p::RFP* or *ttx-3p::GFP* at 50 ng/μL (see Tables S2 and S3). At least two independent transgenic lines were analyzed for each construct.

Fluorescent Microscopy

Fluorescent reporters were used to visualize and evaluate the morphology of ALM, PLM, and PVD neurons. Neuron morphology was phenotyped with a Zeiss Axio Imager M2 using 0.5 to 1% M9 dilution of 1-phenoxy-2-propanol (Fisher, P011825ML) to immobilize the animals. Representative images were collected with a Leica SP8 upright confocal microscope, using polystyrene beads (Polysciences, 00876-15, 0.1 μM diameter) to immobilize the animals (Kim et al., 2013). Confocal images shown are projections of Z-stack images (0.5-1μm/slice) collected using 63X objective.

Quantification of Neuron Morphological Defects

<u>PVD neurons</u>

wdIs51 (F49H12.4::GFP) (Smith et al., 2010) was used to visualize PVD neurons. PVD excessive dendritic branching was assessed by quantifying the number of 5° and 6° branches. 5° branches were identified based on the established dendritic structure of the PVD, with 1° branches emerging from the soma, 2° branches emerging from the 1°, and 3° and 4° following the same pattern and forming 'menorah' units. 5° and 6° branches also follow this pattern and are observed within these 'menorah' (Fig. 1B). The number of 5° and 6° branches for each animal were counted for either the right or left PVD neuron for either the dorsal or ventral side, depending on which was clearly visible during the imaging session. For the assessment of the PVD dendritic beading phenotype, we quantified the number of bead- or bubble-like structures present along the dendrites of either PVDL or PVDR across the entire dendritic tree for each animal. An animal was considered as having the degenerative phenotype only if a total of ten or more bead- or bubble-like structures were observed in over five PVD menorahs (E et al.,

2018). For severity quantification in Figure 5A, an animal with 0-10 beading structures was scored as normal, 10-20 mild, 20-50 moderate, and >50 was scored as severe. In Figure S1B, a more detailed scoring system was employed: a score of 1 indicated 0-10 structures; 2 indicated 10-20; 3 indicated 20-30; 4 indicated 30-50; 5 indicated 50-100; 6 indicated 100-200; and 7 indicated more than 200 structures, or a number beyond countable. An extrachromosomal array of *ser-2(3)p::mCherry-PH* was also used to visualize the membrane structures of PVD dendrites with respect to PVD dendritic F-actin dynamics. *ser-2(3)p::GFP (lxyEx77)* was constructed to visualize PVD neurons when examining *rig-3* mutant animals, due to the difficulty in crossing *rig-3(ok2156)X* into *wdIs51 (F49H12.4::GFP)X*. The *ser-2(3)p::GFP (lxyEx77)* animals exhibited a larger body size than *wdIs51 (F49H12.4::GFP)*, likely due to different genetic backgrounds, which may explain the variation in branching numbers observed in the two PVD reporter strains at Day 1 of adulthood.

ALM/PLM neurons

zdIs5 (mec-4p::GFP) (Clark & Chiu, 2003) was used to visualize ALM and PLM neurons. To quantify the abnormal branching phenotype, the number of ectopic branches sprouting from their main neurites were counted.

Data collection

For each experimental group, a minimum of three independent replicates of 30 animals were always quantified alongside a control group in parallel to mitigate inherent variability. Experimenters scoring and analyzing assays were also blinded to the grouping information to reduce bias.

PVD Function Analysis: Harsh Touch Response

The measurement of the harsh touch response was conducted as previously described (Chalfie & Sulston, 1981; E et al., 2018; Li et al., 2011; Way & Chalfie, 1989), with modifications to the scoring system. The PVD neurons in *C. elegans* are essential for mediating responses to harsh touch stimuli applied to the mid-body, typically triggering either forward or backward locomotion (Chatzigeorgiou et al., 2010; Li et al., 2011; Way & Chalfie, 1989). Since gentle touch activation of touch receptor neurons such as ALM, AVM, PLM, and PVM can induce similar behavioral reactions (Way & Chalfie, 1989), to isolate the role of PVD neurons from the influence of other touch receptor neurons in our assays, we employed a *mec-4(u253)* mutant background with non-functional touch receptor neurons but intact PVD neuron functionality (Driscoll & Chalfie, 1991; Liu & Shen, 2011). *mec-3(e1338)* mutants, which lack normal functioning in both PVD and other touch receptor neurons, were used as a positive control for ‘no harsh touch response’ (E et al., 2018; Liu & Shen, 2011; Way & Chalfie, 1989). Briefly, to measure the harsh touch response, a worm pick was used to gently prod the midsection of minimally moving animals. The elicited escape movement, either forward or reverse, was observed within 5 seconds following the touch. Scoring was based on the distance moved: a score of 1 was assigned if the animal moved more than one body length, a score of 0.5 if it moved between one-third and one body length, and a score of 0 if it did not move or moved less than one-third of a body length. Each animal underwent 10 trials, with intervals of 10-15 minutes between trials. The cumulative score from all trials ranged from 0, indicating severely impaired harsh touch response, to 10, denoting an optimal response.

PVD Function Analysis: Proprioception

Proprioceptive sensing specific to PVD neurons was assessed using a locomotion assay as described previously (Tavernarakis et al., 1997) (Tao et al., 2019) with some modifications. On the day of assay, animals were transferred to fresh NGM plates seeded with OP50, one animal per plate, and allowed to roam freely for 2-3 hours at 20 ^{o}C, until sufficient tracks were made in the bacterial lawn. The plate was then imaged using a digital camera attached to a Leica S9i stereomicroscope at 1X magnification. Three independent replicates of 10 animals each were assayed for each group. A total of 100 randomly selected wavelengths (distance between two adjacent peaks) and amplitudes (distance between peak and wavelength, perpendicular to wavelength) were measured using Fiji. All measurements were used in cases where animals had fewer than 100 measurements, with a minimum of 40 measurements per animal. All measurements were normalized to the body lengths of individual animals and units were converted to millimeters utilizing a reference slide. All animals subjected to proprioception assay were also examined under the Zeiss to quantify PVD dendritic branching.

Reverse Transcription-quantitative PCR

TRI reagent method

To quantify the change in expression level of collagens in aging, N2 WT animals at Day 1 and Day 7 of adulthood were collected. Animals were washed with M9 solution for three 30-minute washes, and total RNA was isolated with TRI reagent (Millipore Sigma, 93289-100mL).

10-worm lysis method

To test the efficiency of RNAi knockdown experiments, 10-worm lysis method (Ly et al., 2015) was used to prepare RNA samples from animals subjected to RNAi treatment. Briefly, 10 worms from each RNAi treatment group were collected and cleaned in H_2O before depositing in 1 μL of lysis buffer (0.25 mM EDTA (Merck), 5mM Tris pH 8.0 (Sigma-Aldrich), 0.5% Triton X-100, 0.5% Tween-20 1mg/mL proteinase K) (Ly et al., 2015). The samples then underwent a lysis cycle via incubating in a thermal cycler for 15 minutes at 65 ^{o}C followed by 1 minute at 85 ^{o}C and storing at -80 ^{o}C for at least 12 hours. Following this, 1.5 μL of additional lysis buffer was added to the original sample and incubated with the same lysis cycle. The lysed samples were then treated with dsDNAse (ThermoFisher, EN0771) by adding 0.5 μL each of 10X dsDNAse buffer and dsDNAse, 1.5 μL of ultrapure H_2O, and then incubating at 37 ^{o}C for 15 minutes, 55 ^{o}C for 5 minutes, and 65 ^{o}C for 1 minute. The samples were then processed to reverse transcription.

Reverse transcription was performed with iScript Reverse Transcription Supermix for RT-qPCR (BioRad, 1708841). Quantitative real-time reverse transcription PCR was performed using TaqMan Gene Expression Assays (ThermoFisher, Ce02462726_m1, Ce02417736_s1, Ce02457574_g1) and iTaq Universal Probes Supermix (Bio-Rad, 1725131) to quantify the mRNA levels of *dpy-5* and *col-120,* and *ama-1* was used as a housekeeping control. Bio Rad CFX96 Touch Deep Well Real-time PCR Detection System was used to perform the qPCR and relative mRNA levels were calculated using comparative ΔΔCT method.

Lifespan Assay

Lifespan assay was performed using 30 animals per replicate for 3 independent replicates. L4 animals were transferred to 100 μM FUDR plates and scored daily. An animal was considered dead when it no longer responded to gentle prodding with a platinum wire and displayed a lack

of pharyngeal pumping. Lifespan was calculated from the time animals were placed on the FUDR plates until they were scored as dead. Animals that died due to protruding/bursting vulva, internal hatching, as well as animals that crawled off the agar were censored.

PVD Time-lapse Imaging and Analysis

The PVD higher-order branches in young adults are highly dynamic structures (Smith et al., 2010). Time-lapse imaging was performed utilizing the Leica SP8 upright confocal microscope, using polystyrene beads and 2% agarose pads to immobilize the animals (Kim et al., 2013). Control animals *[lxyEx51 (ser2(3)p::mCherry-PH; ser2(3)p::GFP::UtrCH)]* were imaged at Day 1 and Day 9 of adulthood. Each imaging session was 8 minutes long with 2-minute intervals, and the images are projections of Z-stack images collected using 63X objective using both the red and green channels. The branch dynamics were quantified using Fiji to measure the length of individual higher-order branches at every imaging time-point. An assessment of the actin dynamics was made by visually assessing the movement of the GFP-labelled actin in the higher-order branches.

Adulthood-specific RNAi

For RNAi experiments, we used the feeding method, where *E. coli* HT115(DE3) carrying either the empty L4440 double T7 vector or the vector producing dsRNA for the gene of interest is fed to *C. elegans* as food (Conte et al., 2015). NGM plates containing isopropylthiogalactoside (IPTG) (Millipore Sigma, I6758-5G) were utilized to induce dsRNA expression. FUDR at a concentration of 100 μM was externally added to these plates following growth of the HT115 bacterial lawn. For RNAi knockdown of genes of interest, CT animals (or mutant animals, as indicated in Results) at mid-L4 or late L4 stage were transferred onto RNAi plates seeded with HT115 bacteria expressing the appropriate dsRNA. The dendritic branching of the PVD neuron, and the proprioception of the animals were assessed 72 hours later at Day 3 of adulthood. The RNAi clones were created using PCR from cDNA or obtained from the Vidal RNAi library (distributed by Horizon Discovery, Key Resources Table). Prior to treating animals, all RNAi clones were sequenced to verify their identities. Empty L4440 plasmid was utilized as a negative control. TJ356 *[zIs356 (daf-16p::daf-16a/b::GFP)]* animals with empty-vector or *daf-2* RNAi treatment were utilized as a positive control. If the RNAi treatment was successful, the *daf-2* RNAi treated animals would display nuclear translocation of DAF-16::GFP, if unsuccessful, the DAF-16::GFP would remain in the cytoplasm (Henderson & Johnson, 2001).

Gene expression datasets and pathway enrichment analyses

Publicly available gene expression datasets were obtained from the Gene Expression Omnibus (Barrett et al., 2013; Edgar et al., 2002). To assess the expression changes of collagen genes during normal aging, we analyzed the RNA-seq transcriptomic dataset GSE176088 (Sheng & Xiao, 2021), which includes three samples from L4 N2/wild-type worms and three samples from Day 10 N2 worms, all maintained at 20°C, using the online tool GEO2R. To gain insights into the potential downstream mechanisms by which skin cuticular collagens influence neuronal integrity, we analyzed microarray profiling data (GSE19310) from N2 and *dpy-10(e128)* mutant worms at the young adult stage (Rohlfing et al., 2010), using GEO2R to identify differentially expressed genes (DEGs). Genes with log2-fold change ≥ 1.5 and a *p*-value < 0.05 were considered as DEGs. The biological functions of the downregulated genes in *dpy-10(e128)* mutant worms were further explored through Kyoto Encyclopedia of

Genes and Genomes (KEGG) enrichment analysis (Kanehisa & Goto, 2000) using the Database for Annotation, Visualization and Integrated Discovery (DAVID, version 2021) (Huang et al., 2007; Sherman et al., 2022). A false discovery rate (FDR) < 0.01 was applied as the threshold for statistical significance. The top 10 significant KEGG pathways were visualized in a bubble graph, where the Rich factor represents the ratio of DEGs annotated within a specific pathway term to the total number of genes annotated in that pathway.

Statistical Analysis

All data processing, statistical analyses, and graph plotting were performed with GraphPad Prism software. Prior to statistical testing, the normality of datasets was assessed using the D'Agostino & Pearson test. For comparisons between an experimental and a control group, we used an unpaired t-test with Welch's correction for normally distributed data, and the Mann-Whitney test for non-normally distributed data. When comparing three or more groups, either one-way ANOVA or the Kruskal-Wallis test (non-parametric), followed by Dunn's multiple comparisons post-hoc analysis. Pearson's correlation test was applied for correlation analyses. Log-Rank test was used to analyze lifespan data. Bar graphs display the mean ± SEM for normally distributed data, and the median with interquartile range for non-normally distributed data.

Table S2

Strain	**Genotype**	**Notes**
N2	Wild type	CGC
NC1686	*F49H12.4::GFP;unc-119(+)(wdIs51)X*	CGC, used to create ELZ55
BC10008	*dpy-5(e907) I; sEx10008*	CGC, used to create ELZ23
CB128	*dpy-10(e128) II;*	CGC, used to create ELZ43
CZ10175	*zdIs5 [mec-4p::GFP + lin-15(+)] I*	CGC
PS8819	*col-120(sy1526)IV*	CGC, used to create ELZ60
RB1712	*rig-3(ok2156) X*	CGC, used to create ELZ155
TJ356	*zIs356 [daf-16p::DAF-16a/b::GFP; rol-6] IV*	CGC
ELZ23	*dpy-5(e907) I; F49H12.4::GFP;unc-119(+)(wdIs51)X*	-
ELZ30	*zdIs5 [mec-4p::GFP + lin-15(+)] I; dpy-5(e907) I*	-
ELZ43	*dpy-10(e128) II; F49H12.4::GFP; unc-119(+)(wdIs51) X*	-
ELZ55	*F49H12.4::GFP; unc-119(+)(wdIs51) X*	1x outcross of NC1686
ELZ60	*col-120(sy1526)IV; F49H12.4::GFP;unc-119(+)(wdIs51)X*	-
ELZ78	*F49H12.4::GFP;unc-119(+)(wdIs51)X; dpy-30p::col-120 cDNA(lxyEx16)*	100ng/μL PELZ32 + 50ng/μL PELZ5 into ELZ55
ELZ76	*F49H12.4::GFP;unc-119(+)(wdIs51)X; dpy-30p::col-120 cDNA(lxyEx14)*	100ng/μL PELZ32 + 50ng/μL PELZ5 into ELZ55
ELZ83	*col-120(sy1526)IV; F49H12.4::GFP;unc-119(+)(wdIs51)X; dpy-30p::col-120 cDNA(lxyEx21)*	10ng/μL PELZ32 + 50ngμL PELZ5 into ELZ60

ELZ86	*F49H12.4::GFP;unc-119(+)(wdIs51)X; col-19p::dpy-5 gDNA (lxyEx24)*	100 ng/μL PELZ19 into ELZ55
ELZ90	*col-120(sy1526)IV; F49H12.4::GFP;unc-119(+)(wdIs51)X; dpy7p::col120+ col-19p::col120(lxyEx26)*	20ng/μL PELZ31 + 20 ng/μL PELZ37 + 50 ng/μL PELZ5 into ELZ60
ELZ121	*ser-2(3)p::EMTB::GFP + ser-2(3)p::mCherry-PH(lxyEx48)*	4ng/μL PNYL931 + 4ng/μL PNYL720 + 50ng/μL PELZ5 to inN2
ELZ124	*ser-2(3)p::GFP::UtrCH + ser-2(3)p::mCherry-PH(lxyEx51)*	4 ng/μL PNYL930 + 6ng/μL PNYL720 + 50 ng/μL PELZ5 into N2
ELZ132	*dpy-5(e907)I; F49H12.4::GFP;unc-119(+)(wdIs51)X; dpy-7p::dpy5(lxyEx57)*	30 ng/μL PELZ75 + 50 ng/μL PELZ5 into ELZ23
ELZ133	*dpy-5 (e907)I; F49H12.4::GFP;unc-119(+)(wdIs51)X; dpy-7p::dpy-5 cDNA (lxyEx58)*	30 ng/μL PELZ75 + 50 ng/μL PELZ5 into ELZ23
ELZ150	*col-120(sy1526)IV; F49H12.4::GFP;unc-119(+)(wdIs51)X*	10 ng/μL PELZ37+ 50 ng/μL PELZ5 into ELZ60
ELZ155	*rig-3(ok2156) X*	4X outcross of RB1712
ELZ161	*ser-2(3)p::GFP (lxyEx77)*	10 ng/μL PELZ47+ 50 ng/μL PELZ4 into N2
ELZ166	*rig-3(ok2156)X; ser-2(3)p::GFP (lxyEx77)*	ELZ161 crossed with ELZ155

Table S3

Plasmid number	**Plasmid description**
PELZ4	*ttx-3p::GFP*
PNYL720	*ser-2(3)p::mCherry-PH*
PNYL930	*ser-2(3)p::GFP-UtrCH*
PNYL931	*ser-2(3)p::EMTB::GFP*
PELZ5	*ttx-3p::RFP*
PELZ19	*col-19p::dpy-5 cDNA*
PELZ31	*dpy-7p::col-120*
PELZ32	*dpy-30p::col120 cDNA*
PELZ37	*col-19p::col-120 cDNA*
PELZ44	*col-120::L4440*
PELZ45	*col-120(1)::L4440*
PELZ46	*col-120(2)::L4440*
PELZ47	*ser-2(3)p::GFP*
PELZ48	*dpy-5::L4440*
PELZ75	*dpy-7p (unc-54 3'UTR)::dpy-5*
C. elegans RNAi feeding library, Horizon Discovery	*L4440::rig-3*
C. elegans RNAi feeding library, Horizon Discovery	*L4440::ina-1*
C. elegans RNAi feeding library, Horizon Discovery	*L4440::ddr-2*
C. elegans RNAi feeding library, Horizon Discovery	*L4440::sdn-1*

Table S4

Primer name	Primer sequence (5'-3')	Purpose
ok2156 Forward 1.4	CGTCATTTCATCAGAAGCCATG	Forward genotyping primer for *rig-3(ok2156)*
ok2156 Reverse 1.2	CCTGTAATAGAGTCGTTTACAACTT GTTTC	Reverse genotyping primer for *rig-3(ok2156)*
ok2156 Reverse 2	GTCATCTGAATCATTGGTTCTTTAC	Reverse genotyping primer for *rig-3(ok2156)*
Dpy-5-For	TTA GAC GCG TCT GCG CTT TCT CTC TG	Forward primer for *dpy-5* cDNA amplification
Dpy-5-Rev	ATGGTAAAGGCCGTCGTCGGATTCG	Reverse primer for *dpy-5* cDNA amplification
dpy-5(e907)-F1	GAAGCATGGGTCTCGTTAG	Forward genotyping primer for *dpy-5*
dpy-5(e907)-F2	GTCCTGGAGTTCCTTGATC	Forward genotyping primer for *dpy-5*
dpy-5(e907)-R	GAAGGTGTGTCCTCATGG	Reverse genotyping primer for *dpy-5*
Col-120 For	ATGAATTTGAAGAAGAATTTAGTGAA TTCTGAAGAGGATG	Forward primer for *col-120* cDNA amplification
Col-120 Rev	TTAGTATCCAGGAGCAGTTCGTGGA GGTG	Reverse primer for *col-120* cDNA amplification
Col-120(sy2156)-F	GTTGCTTTCGTGGCGACTG	Forward genotyping primer for *col-120*
Col-120(sy2156)-R	CCTCCATATCCAGCTTGTC	Reverse genotyping primer for *col-120*
rig-3 For	ATGGGACGACTACTTGCCAAGATG	Forward primer for *rig-3* cDNA amplification
rig-3 Rev	TTAGATAAAAAGACAGACAAAAAATA ACGTG	Reverse primer for *rig-3* cDNA amplification

REFERENCES

Albeg, A., Smith, C. J., Chatzigeorgiou, M., Feitelson, D. G., Hall, D. H., Schafer, W. R., Miller, D. M., 3rd, & Treinin, M. (2011). C. elegans multi-dendritic sensory neurons: morphology and function. *Mol Cell Neurosci*, *46*(1), 308-317. https://doi.org/10.1016/j.mcn.2010.10.001

Ashford, J. W., Soultanian, N. S., Zhang, S. X., & Geddes, J. W. (1998). Neuropil threads are collinear with MAP2 immunostaining in neuronal dendrites of Alzheimer brain. *J Neuropathol Exp Neurol*, *57*(10), 972-978. https://doi.org/10.1097/00005072-199810000-00009

Babu, K., Hu, Z., Chien, S. C., Garriga, G., & Kaplan, J. M. (2011). The immunoglobulin super family protein RIG-3 prevents synaptic potentiation and regulates Wnt signaling. *Neuron*, *71*(1), 103-116. https://doi.org/10.1016/j.neuron.2011.05.034

Barrett, T., Wilhite, S. E., Ledoux, P., Evangelista, C., Kim, I. F., Tomashevsky, M., Marshall, K. A., Phillippy, K. H., Sherman, P. M., Holko, M., Yefanov, A., Lee, H., Zhang, N., Robertson, C. L., Serova, N., Davis, S., & Soboleva, A. (2013). NCBI GEO: archive for functional genomics data sets--update. *Nucleic Acids Res*, *41*(Database issue), D991-995. https://doi.org/10.1093/nar/gks1193

Bergman, E., Ulfhake, B., & Fundin, B. T. (2000). Regulation of NGF-family ligands and receptors in adulthood and senescence: correlation to degenerative and regenerative changes in cutaneous innervation. *Eur J Neurosci*, *12*(8), 2694-2706. https://doi.org/10.1046/j.1460-9568.2000.00149.x

Berkowitz, L. A., Knight, A. L., Caldwell, G. A., & Caldwell, K. A. (2008). Generation of stable transgenic C. elegans using microinjection. *J Vis Exp*(18). https://doi.org/10.3791/833

Bhardwaj, A., Pandey, P., & Babu, K. (2020). Control of Locomotory Behavior of. *Genetics*, *214*(1), 135-145. https://doi.org/10.1534/genetics.119.302872

Bouche, P. (2020). Neuropathy of the elderly. *Rev Neurol (Paris)*, *176*(9), 733-738. https://doi.org/10.1016/j.neurol.2019.11.007

Brenner, S. (1974). The genetics of Caenorhabditis elegans. *Genetics*, *77*(1), 71-94. https://doi.org/10.1093/genetics/77.1.71

Burkel, B. M., von Dassow, G., & Bement, W. M. (2007). Versatile fluorescent probes for actin filaments based on the actin-binding domain of utrophin. *Cell Motil Cytoskeleton*, *64*(11), 822-832. https://doi.org/10.1002/cm.20226

Callisaya, M. L., Blizzard, L., Schmidt, M. D., McGinley, J. L., & Srikanth, V. K. (2010). Ageing and gait variability--a population-based study of older people. *Age Ageing*, *39*(2), 191-197. https://doi.org/10.1093/ageing/afp250

Castelli, G., Desai, K. M., & Cantone, R. E. (2020). Peripheral Neuropathy: Evaluation and Differential Diagnosis. *Am Fam Physician*, *102*(12), 732-739. https://www.ncbi.nlm.nih.gov/pubmed/33320513

Cescon, M., Chen, P., Castagnaro, S., Gregorio, I., & Bonaldo, P. (2016). Lack of collagen VI promotes neurodegeneration by impairing autophagy and inducing apoptosis during aging. *Aging (Albany NY)*, *8*(5), 1083-1101. https://doi.org/10.18632/aging.100924

Chalfie, M., & Sulston, J. (1981). Developmental genetics of the mechanosensory neurons of Caenorhabditis elegans. *Dev Biol*, *82*(2), 358-370. https://doi.org/10.1016/0012-1606(81)90459-0

Chatzigeorgiou, M., Yoo, S., Watson, J. D., Lee, W. H., Spencer, W. C., Kindt, K. S., Hwang, S. W., Miller, D. M., Treinin, M., Driscoll, M., & Schafer, W. R. (2010). Specific roles for DEG/ENaC and TRP channels in touch and thermosensation in C. elegans nociceptors. *Nat Neurosci*, *13*(7), 861-868. https://doi.org/10.1038/nn.2581

Chen, Y. L., Tao, J., Zhao, P. J., Tang, W., Xu, J. P., Zhang, K. Q., & Zou, C. G. (2019). Adiponectin receptor PAQR-2 signaling senses low temperature to promote C. elegans longevity by regulating autophagy. *Nat Commun*, *10*(1), 2602. https://doi.org/10.1038/s41467-019-10475-8

Chia, P. H., Chen, B., Li, P., Rosen, M. K., & Shen, K. (2014). Local F-actin network links synapse formation and axon branching. *Cell*, *156*(1-2), 208-220. https://doi.org/10.1016/j.cell.2013.12.009

Chisholm, A. D., & Hsiao, T. I. (2013). The *C. elegans* epidermis as a model skin. I: development, patterning, and growth. *Wiley Interdiscip Rev Dev Biol.* .

Chisholm, A. D., & Xu, S. (2012). The Caenorhabditis elegans epidermis as a model skin. II: differentiation and physiological roles. *Wiley Interdiscip Rev Dev Biol*, *1*(6), 879-902. https://doi.org/10.1002/wdev.77

Chiu, H., Zou, Y., Suzuki, N., Hsieh, Y. W., Chuang, C. F., Wu, Y. C., & Chang, C. (2018). Engulfing cells promote neuronal regeneration and remove neuronal debris through distinct biochemical functions of CED-1. *Nat Commun*, *9*(1), 4842. https://doi.org/10.1038/s41467-018-07291-x

Clark, S. G., & Chiu, C. (2003). C. elegans ZAG-1, a Zn-finger-homeodomain protein, regulates axonal development and neuronal differentiation. *Development*, *130*(16), 3781-3794. https://doi.org/10.1242/dev.00571

Conte, D., Jr., MacNeil, L. T., Walhout, A. J. M., & Mello, C. C. (2015). RNA Interference in Caenorhabditis elegans. *Curr Protoc Mol Biol*, *109*, 26 23 21-26 23 30. https://doi.org/10.1002/0471142727.mb2603s109

Correia, C., Lopez, K. J., Wroblewski, K. E., Huisingh-Scheetz, M., Kern, D. W., Chen, R. C., Schumm, L. P., Dale, W., McClintock, M. K., & Pinto, J. M. (2016). Global Sensory Impairment in Older Adults in the United States. *J Am Geriatr Soc*, *64*(2), 306-313. https://doi.org/10.1111/jgs.13955

Corsi, A. K., Wightman, B., & Chalfie, M. (2015). A Transparent window into biology: A primer on Caenorhabditis elegans. *WormBook*, 1-31. https://doi.org/10.1895/wormbook.1.177.1

Cuentas-Condori, A., Mulcahy, B., He, S., Palumbos, S., Zhen, M., & Miller, D. M. (2019). neurons have functional dendritic spines. *Elife*, *8*. https://doi.org/10.7554/eLife.47918

Davis, P., Zarowiecki, M., Arnaboldi, V., Becerra, A., Cain, S., Chan, J., Chen, W. J., Cho, J., da Veiga Beltrame, E., Diamantakis, S., Gao, S., Grigoriadis, D., Grove, C. A., Harris, T. W., Kishore, R., Le, T., Lee, R. Y. N., Luypaert, M., Müller, H. M., Nakamura, C., Nuin, P., Paulini, M., Quinton-Tulloch, M., Raciti, D., Rodgers, F. H., Russell, M., Schindelman, G., Singh, A., Stickland, T., Van Auken, K., Wang, Q., Williams, G., Wright, A. J., Yook, K., Berriman, M., Howe, K. L., Schedl, T., Stein, L., & Sternberg, P. W. (2022). WormBase in 2022-data, processes, and tools for analyzing Caenorhabditis elegans. *Genetics*, *220*(4). https://doi.org/10.1093/genetics/iyac003

Dodd, W., Tang, L., Lone, J. C., Wimberly, K., Wu, C. W., Consalvo, C., Wright, J. E., Pujol, N., & Choe, K. P. (2018). A Damage Sensor Associated with the Cuticle Coordinates Three Core Environmental Stress Responses in. *Genetics*, *208*(4), 1467-1482. https://doi.org/10.1534/genetics.118.300827

Dong, X., Liu, O. W., Howell, A. S., & Shen, K. (2013). An extracellular adhesion molecule complex patterns dendritic branching and morphogenesis. *Cell*, *155*(2), 296-307. https://doi.org/10.1016/j.cell.2013.08.059

Driscoll, M., & Chalfie, M. (1991). The mec-4 gene is a member of a family of Caenorhabditis elegans genes that can mutate to induce neuronal degeneration. *Nature*, *349*(6310), 588-593. https://doi.org/10.1038/349588a0

E, L., Zhou, T., Koh, S., Chuang, M., Sharma, R., Pujol, N., Chisholm, A. D., Eroglu, C., Matsunami, H., & Yan, D. (2018). An Antimicrobial Peptide and Its Neuronal Receptor Regulate Dendrite Degeneration in Aging and Infection. *Neuron*, *97*(1), 125-138.e125. https://doi.org/10.1016/j.neuron.2017.12.001

Edgar, R., Domrachev, M., & Lash, A. E. (2002). Gene Expression Omnibus: NCBI gene expression and hybridization array data repository. *Nucleic Acids Res*, *30*(1), 207-210. https://doi.org/10.1093/nar/30.1.207

Ewald, C. Y., Landis, J. N., Porter Abate, J., Murphy, C. T., & Blackwell, T. K. (2015). Dauer-independent insulin/IGF-1-signalling implicates collagen remodelling in longevity. *Nature*, *519*(7541), 97-101. https://doi.org/10.1038/nature14021

Faerman, I., Faccio, E., Calb, I., Razumny, J., Franco, N., Dominguez, A., & Podesta, H. A. (1982). Autonomic neuropathy in the skin: a histological study of the sympathetic nerve fibres in diabetic anhidrosis. *Diabetologia*, *22*(2), 96-99. https://doi.org/10.1007/BF00254836

Fatima, I., Chen, G., Botchkareva, N. V., Sharov, A. A., Thornton, D., Wilkinson, H. N., Hardman, M. J., Grutzkau, A., Pedro de Magalhaes, J., Seluanov, A., Smith, E. S. J., Gorbunova, V., Mardaryev, A. N., Faulkes, C. G., & Botchkarev, V. A. (2022). Skin Aging in Long-Lived Naked Mole-Rats Is Accompanied by Increased Expression of Longevity-Associated and Tumor Suppressor Genes. *J Invest Dermatol*, *142*(11), 2853-2863 e2854. https://doi.org/10.1016/j.jid.2022.04.028

Feng, X., Guo, J., Sigmon, H. C., Sloan, R. P., Brickman, A. M., Provenzano, F. A., Small, S. A., & Alzheimer's Disease Neuroimaging, I. (2020). Brain regions vulnerable and resistant to aging without Alzheimer's disease. *PLoS One*, *15*(7), e0234255. https://doi.org/10.1371/journal.pone.0234255

Glenn, C. F., Chow, D. K., David, L., Cooke, C. A., Gami, M. S., Iser, W. B., Hanselman, K. B., Goldberg, I. G., & Wolkow, C. A. (2004). Behavioral deficits during early stages of aging in Caenorhabditis elegans result from locomotory deficits possibly linked to muscle frailty. *J Gerontol A Biol Sci Med Sci*, *59*(12), 1251-1260. https://doi.org/10.1093/gerona/59.12.1251

Goodness, T. P., Albers, K. M., Davis, F. E., & Davis, B. M. (1997). Overexpression of nerve growth factor in skin increases sensory neuron size and modulates Trk receptor expression. *Eur J Neurosci*, *9*(8), 1574-1585. https://doi.org/10.1111/j.1460-9568.1997.tb01515.x

Halevi, S., McKay, J., Palfreyman, M., Yassin, L., Eshel, M., Jorgensen, E., & Treinin, M. (2002). The C. elegans ric-3 gene is required for maturation of nicotinic acetylcholine receptors. *EMBO J*, *21*(5), 1012-1020. https://doi.org/10.1093/emboj/21.5.1012

Henderson, S. T., & Johnson, T. E. (2001). daf-16 integrates developmental and environmental inputs to mediate aging in the nematode Caenorhabditis elegans. *Curr Biol*, *11*(24), 1975-1980. https://doi.org/10.1016/s0960-9822(01)00594-2

Henry, M., & Baudry, S. (2019). Age-related changes in leg proprioception: implications for postural control. *J Neurophysiol*, *122*(2), 525-538. https://doi.org/10.1152/jn.00067.2019
Hess, M., Gomariz, A., Goksel, O., & Ewald, C. Y. (2019). In-Vivo Quantitative Image Analysis of Age-Related Morphological Changes of C. elegans Neurons Reveals a Correlation between Neurite Bending and Novel Neurite Outgrowths. *eNeuro*, *6*(4). https://doi.org/10.1523/ENEURO.0014-19.2019
Hicks, C. W., Wang, D., Windham, B. G., Matsushita, K., & Selvin, E. (2021). Prevalence of peripheral neuropathy defined by monofilament insensitivity in middle-aged and older adults in two US cohorts. *Sci Rep*, *11*(1), 19159. https://doi.org/10.1038/s41598-021-98565-w
Hobert, O. (2013). The neuronal genome of Caenorhabditis elegans. *WormBook*, 1-106. https://doi.org/10.1895/wormbook.1.161.1
Huang, D. W., Sherman, B. T., Tan, Q., Kir, J., Liu, D., Bryant, D., Guo, Y., Stephens, R., Baseler, M. W., Lane, H. C., & Lempicki, R. A. (2007). DAVID Bioinformatics Resources: expanded annotation database and novel algorithms to better extract biology from large gene lists. *Nucleic Acids Res*, *35*(Web Server issue), W169-175. https://doi.org/10.1093/nar/gkm415
Hunter, S. K., Pereira, H. M., & Keenan, K. G. (2016). The aging neuromuscular system and motor performance. *J Appl Physiol (1985)*, *121*(4), 982-995. https://doi.org/10.1152/japplphysiol.00475.2016
Huntley, M. A., Srinivasan, K., Friedman, B. A., Wang, T. M., Yee, A. X., Wang, Y., Kaminker, J. S., Sheng, M., Hansen, D. V., & Hanson, J. E. (2020). Genome-Wide Analysis of Differential Gene Expression and Splicing in Excitatory Neurons and Interneuron Subtypes. *J Neurosci*, *40*(5), 958-973. https://doi.org/10.1523/JNEUROSCI.1615-19.2019
Husson, S. J., Costa, W. S., Wabnig, S., Stirman, J. N., Watson, J. D., Spencer, W. C., Akerboom, J., Looger, L. L., Treinin, M., Miller, D. M., 3rd, Lu, H., & Gottschalk, A. (2012). Optogenetic analysis of a nociceptor neuron and network reveals ion channels acting downstream of primary sensors. *Curr Biol*, *22*(9), 743-752. https://doi.org/10.1016/j.cub.2012.02.066
Jiang, N., Rasmussen, J. P., Clanton, J. A., Rosenberg, M. F., Luedke, K. P., Cronan, M. R., Parker, E. D., Kim, H. J., Vaughan, J. C., Sagasti, A., & Parrish, J. Z. (2019). A conserved morphogenetic mechanism for epidermal ensheathment of nociceptive sensory neurites. *Elife*, *8*. https://doi.org/10.7554/eLife.42455
Jin, M., Shepardson, N., Yang, T., Chen, G., Walsh, D., & Selkoe, D. J. (2011). Soluble amyloid beta-protein dimers isolated from Alzheimer cortex directly induce Tau hyperphosphorylation and neuritic degeneration. *Proc Natl Acad Sci U S A*, *108*(14), 5819-5824. https://doi.org/10.1073/pnas.1017033108
Johnstone, I. L. (2000). Cuticle collagen genes. Expression in Caenorhabditis elegans. *Trends Genet*, *16*(1), 21-27. https://doi.org/10.1016/s0168-9525(99)01857-0
Kaech, S., Parmar, H., Roelandse, M., Bornmann, C., & Matus, A. (2001). Cytoskeletal microdifferentiation: a mechanism for organizing morphological plasticity in dendrites. *Proc Natl Acad Sci U S A*, *98*(13), 7086-7092. https://doi.org/10.1073/pnas.111146798
Kanehisa, M., & Goto, S. (2000). KEGG: kyoto encyclopedia of genes and genomes. *Nucleic Acids Res*, *28*(1), 27-30. https://doi.org/10.1093/nar/28.1.27

Kasai, H., Matsuzaki, M., Noguchi, J., Yasumatsu, N., & Nakahara, H. (2003). Structure-stability-function relationships of dendritic spines. *Trends Neurosci*, *26*(7), 360-368. https://doi.org/10.1016/S0166-2236(03)00162-0

Kehlet, S. N., Willumsen, N., Armbrecht, G., Dietzel, R., Brix, S., Henriksen, K., & Karsdal, M. A. (2018). Age-related collagen turnover of the interstitial matrix and basement membrane: Implications of age- and sex-dependent remodeling of the extracellular matrix. *PLoS One*, *13*(3), e0194458. https://doi.org/10.1371/journal.pone.0194458

Kenyon, C. J. (2010). The genetics of ageing. *Nature*, *464*(7288), 504-512. https://doi.org/10.1038/nature08980

Kim, E., Sun, L., Gabel, C. V., & Fang-Yen, C. (2013). Long-term imaging of Caenorhabditis elegans using nanoparticle-mediated immobilization. *PLoS One*, *8*(1), e53419. https://doi.org/10.1371/journal.pone.0053419

Klass, M. R. (1977). Aging in the nematode Caenorhabditis elegans: major biological and environmental factors influencing life span. *Mech Ageing Dev*, *6*(6), 413-429. https://doi.org/10.1016/0047-6374(77)90043-4

Ko, S. U., Simonsick, E. M., Deshpande, N., Studenski, S., & Ferrucci, L. (2016). Ankle Proprioception-Associated Gait Patterns in Older Adults: Results from the Baltimore Longitudinal Study of Aging. *Med Sci Sports Exerc*, *48*(11), 2190-2194. https://doi.org/10.1249/MSS.0000000000001017

Kramer, J. M., Johnson, J. J., Edgar, R. S., Basch, C., & Roberts, S. (1988). The sqt-1 gene of C. elegans encodes a collagen critical for organismal morphogenesis. *Cell*, *55*(4), 555-565. https://doi.org/10.1016/0092-8674(88)90214-0

Kravtsov, V., Oren-Suissa, M., & Podbilewicz, B. (2017). The fusogen AFF-1 can rejuvenate the regenerative potential of adult dendritic trees by self-fusion. *Development*, *144*(13), 2364-2374. https://doi.org/10.1242/dev.150037

Krimm, R. F., Davis, B. M., Noel, T., & Albers, K. M. (2006). Overexpression of neurotrophin 4 in skin enhances myelinated sensory endings but does not influence sensory neuron number. *J Comp Neurol*, *498*(4), 455-465. https://doi.org/10.1002/cne.21074

Lanoue, V., & Cooper, H. M. (2019). Branching mechanisms shaping dendrite architecture. *Dev Biol*, *451*(1), 16-24. https://doi.org/10.1016/j.ydbio.2018.12.005

Lauria, G., Holland, N., Hauer, P., Cornblath, D. R., Griffin, J. W., & McArthur, J. C. (1999). Epidermal innervation: changes with aging, topographic location, and in sensory neuropathy. *J Neurol Sci*, *164*(2), 172-178. https://doi.org/10.1016/s0022-510x(99)00063-5

Lauwers, E., Debyser, Z., Van Dorpe, J., De Strooper, B., Nuttin, B., & Baekelandt, V. (2003). Neuropathology and neurodegeneration in rodent brain induced by lentiviral vector-mediated overexpression of alpha-synuclein. *Brain Pathol*, *13*(3), 364-372. https://doi.org/10.1111/j.1750-3639.2003.tb00035.x

Lee, S. J., & Kenyon, C. (2009). Regulation of the longevity response to temperature by thermosensory neurons in Caenorhabditis elegans. *Curr Biol*, *19*(9), 715-722. https://doi.org/10.1016/j.cub.2009.03.041

Li, W., Kang, L., Piggott, B. J., Feng, Z., & Xu, X. Z. (2011). The neural circuits and sensory channels mediating harsh touch sensation in Caenorhabditis elegans. *Nat Commun*, *2*, 315. https://doi.org/10.1038/ncomms1308

Liang, X., Dong, X., Moerman, D. G., Shen, K., & Wang, X. (2015). Sarcomeres Pattern Proprioceptive Sensory Dendritic Endings through UNC-52/Perlecan in C. elegans. *Dev Cell*, *33*(4), 388-400. https://doi.org/10.1016/j.devcel.2015.03.010

Liao, C. P., Li, H., Lee, H. H., Chien, C. T., & Pan, C. L. (2018). Cell-Autonomous Regulation of Dendrite Self-Avoidance by the Wnt Secretory Factor MIG-14/Wntless. *Neuron*, *98*(2), 320-334 e326. https://doi.org/10.1016/j.neuron.2018.03.031

Lippman, J., & Dunaevsky, A. (2005). Dendritic spine morphogenesis and plasticity. *J Neurobiol*, *64*(1), 47-57. https://doi.org/10.1002/neu.20149

Liu, O. W., & Shen, K. (2011). The transmembrane LRR protein DMA-1 promotes dendrite branching and growth in C. elegans. *Nat Neurosci*, *15*(1), 57-63. https://doi.org/10.1038/nn.2978

Liu, X., Guo, X., Niu, L., Li, X., Sun, F., Hu, J., Wang, X., & Shen, K. (2019). Atlastin-1 regulates morphology and function of endoplasmic reticulum in dendrites. *Nat Commun*, *10*(1), 568. https://doi.org/10.1038/s41467-019-08478-6

Ly, K., Reid, S. J., & Snell, R. G. (2015). Rapid RNA analysis of individual Caenorhabditis elegans. *MethodsX*, *2*, 59-63. https://doi.org/10.1016/j.mex.2015.02.002

Martyn, C. N., & Hughes, R. A. (1997). Epidemiology of peripheral neuropathy. *J Neurol Neurosurg Psychiatry*, *62*(4), 310-318. https://doi.org/10.1136/jnnp.62.4.310

Menzies, F. M., Fleming, A., & Rubinsztein, D. C. (2015). Compromised autophagy and neurodegenerative diseases. *Nat Rev Neurosci*, *16*(6), 345-357. https://doi.org/10.1038/nrn3961

Nichols, A. L. A., Meelkop, E., Linton, C., Giordano-Santini, R., Sullivan, R. K., Donato, A., Nolan, C., Hall, D. H., Xue, D., Neumann, B., & Hilliard, M. A. (2016). The Apoptotic Engulfment Machinery Regulates Axonal Degeneration in C. elegans Neurons. *Cell Rep*, *14*(7), 1673-1683. https://doi.org/10.1016/j.celrep.2016.01.050

O'Donnell, K. C., Lulla, A., Stahl, M. C., Wheat, N. D., Bronstein, J. M., & Sagasti, A. (2014). Axon degeneration and PGC-1alpha-mediated protection in a zebrafish model of alpha-synuclein toxicity. *Dis Model Mech*, *7*(5), 571-582. https://doi.org/10.1242/dmm.013185

Oliver, D., Norman, E., Bates, H., Avard, R., Rettler, M., Bénard, C. Y., Francis, M. M., & Lemons, M. L. (2019). Integrins Have Cell-Type-Specific Roles in the Development of Motor Neuron Connectivity. *J Dev Biol*, *7*(3). https://doi.org/10.3390/jdb7030017

Oren-Suissa, M., Hall, D. H., Treinin, M., Shemer, G., & Podbilewicz, B. (2010). The fusogen EFF-1 controls sculpting of mechanosensory dendrites. *Science*, *328*(5983), 1285-1288. https://doi.org/10.1126/science.1189095

Pan, C. L., Peng, C. Y., Chen, C. H., & McIntire, S. (2011). Genetic analysis of age-dependent defects of the Caenorhabditis elegans touch receptor neurons. *Proc Natl Acad Sci U S A*, *108*(22), 9274-9279. https://doi.org/10.1073/pnas.1011711108

Pandey, P., Bhardwaj, A., & Babu, K. (2017). Regulation of WNT Signaling at the Neuromuscular Junction by the Immunoglobulin Superfamily Protein RIG-3 in Caenorhabditis elegans. *Genetics*, *206*(3), 1521-1534. https://doi.org/10.1534/genetics.116.195297

Raiders, S., Black, E. C., Bae, A., MacFarlane, S., Klein, M., Shaham, S., & Singhvi, A. (2021). Glia actively sculpt sensory neurons by controlled phagocytosis to tune animal behavior. *Elife*, *10*. https://doi.org/10.7554/eLife.63532

Raiders, S., Han, T., Scott-Hewitt, N., Kucenas, S., Lew, D., Logan, M. A., & Singhvi, A. (2021). Engulfed by Glia: Glial Pruning in Development, Function, and Injury across Species. *J Neurosci*, *41*(5), 823-833. https://doi.org/10.1523/JNEUROSCI.1660-20.2020

Ramirez-Suarez, N. J., Belalcazar, H. M., Salazar, C. J., Beyaz, B., Raja, B., Nguyen, K. C. Q., Celestrin, K., Fredens, J., Færgeman, N. J., Hall, D. H., & Bülow, H. E. (2019). Axon-Dependent Patterning and Maintenance of Somatosensory Dendritic Arbors. *Dev Cell*, *48*(2), 229-244.e224. https://doi.org/10.1016/j.devcel.2018.12.015

Ricard-Blum, S. (2011). The collagen family. *Cold Spring Harb Perspect Biol*, *3*(1), a004978. https://doi.org/10.1101/cshperspect.a004978

Richardson, C. E., Spilker, K. A., Cueva, J. G., Perrino, J., Goodman, M. B., & Shen, K. (2014). PTRN-1, a microtubule minus end-binding CAMSAP homolog, promotes microtubule function in Caenorhabditis elegans neurons. *Elife*, *3*, e01498. https://doi.org/10.7554/eLife.01498

Rohlfing, A. K., Miteva, Y., Hannenhalli, S., & Lamitina, T. (2010). Genetic and physiological activation of osmosensitive gene expression mimics transcriptional signatures of pathogen infection in C. elegans (GEO accession GSE19310). *PLoS One*, *5*(2), e9010. https://doi.org/10.1371/journal.pone.0009010

Rosenheimer, J. L., & Smith, D. O. (1985). Differential changes in the end-plate architecture of functionally diverse muscles during aging. *J Neurophysiol*, *53*(6), 1567-1581. https://doi.org/10.1152/jn.1985.53.6.1567

Rozario, T., & DeSimone, D. W. (2010). The extracellular matrix in development and morphogenesis: a dynamic view. *Dev Biol*, *341*(1), 126-140. https://doi.org/10.1016/j.ydbio.2009.10.026

Saberi-Bosari, S., Flores, K. B., & San-Miguel, A. (2020). Deep learning-enabled analysis reveals distinct neuronal phenotypes induced by aging and cold-shock. *BMC Biol*, *18*(1), 130. https://doi.org/10.1186/s12915-020-00861-w

Salzberg, Y., Diaz-Balzac, C. A., Ramirez-Suarez, N. J., Attreed, M., Tecle, E., Desbois, M., Kaprielian, Z., & Bulow, H. E. (2013). Skin-derived cues control arborization of sensory dendrites in Caenorhabditis elegans. *Cell*, *155*(2), 308-320. https://doi.org/10.1016/j.cell.2013.08.058

Sandhu, A., Badal, D., Sheokand, R., Tyagi, S., & Singh, V. (2021). Specific collagens maintain the cuticle permeability barrier in Caenorhabditis elegans. *Genetics*, *217*(3). https://doi.org/10.1093/genetics/iyaa047

Saxena, S., & Caroni, P. (2011). Selective neuronal vulnerability in neurodegenerative diseases: from stressor thresholds to degeneration. *Neuron*, *71*(1), 35-48. https://doi.org/10.1016/j.neuron.2011.06.031

Schwarz, V., Pan, J., Voltmer-Irsch, S., & Hutter, H. (2009). IgCAMs redundantly control axon navigation in Caenorhabditis elegans. *Neural Dev*, *4*, 13. https://doi.org/10.1186/1749-8104-4-13

Shaye, D. D., & Greenwald, I. (2015). The disease-associated formin INF2/EXC-6 organizes lumen and cell outgrowth during tubulogenesis by regulating F-actin and microtubule cytoskeletons. *Dev Cell*, *32*(6), 743-755. https://doi.org/10.1016/j.devcel.2015.01.009

Sheng, Y., & Xiao, R. (2021). *Next Generation Sequencing Facilitates Quantitative Analysis of aged (Day10) and young (L4) C. elegans Transcriptomes (NCBI GEO accession GSE176088)*.

Sherman, B. T., Hao, M., Qiu, J., Jiao, X., Baseler, M. W., Lane, H. C., Imamichi, T., & Chang, W. (2022). DAVID: a web server for functional enrichment analysis and functional annotation of gene lists (2021 update). *Nucleic Acids Res*, *50*(W1), W216-W221. https://doi.org/10.1093/nar/gkac194

Smith, C. J., Watson, J. D., Spencer, W. C., O'Brien, T., Cha, B., Albeg, A., Treinin, M., & Miller, D. M. (2010). Time-lapse imaging and cell-specific expression profiling reveal dynamic branching and molecular determinants of a multi-dendritic nociceptor in C. elegans. *Dev Biol*, *345*(1), 18-33. https://doi.org/10.1016/j.ydbio.2010.05.502

Stammers, M., Ivanova, I. M., Niewczas, I. S., Segonds-Pichon, A., Streeter, M., Spiegel, D. A., & Clark, J. (2020). Age-related changes in the physical properties, cross-linking, and glycation of collagen from mouse tail tendon. *J Biol Chem*, *295*(31), 10562-10571. https://doi.org/10.1074/jbc.RA119.011031

Stewart, A., Tsubouchi, A., Rolls, M. M., Tracey, W. D., & Sherwood, N. T. (2012). Katanin p60-like1 promotes microtubule growth and terminal dendrite stability in the larval class IV sensory neurons of Drosophila. *J Neurosci*, *32*(34), 11631-11642. https://doi.org/10.1523/JNEUROSCI.0729-12.2012

Sun, J. H., Huang, M., Fang, Z., Li, T. X., Wu, T. T., Chen, Y., Quan, D. P., Xu, Y. Y., Wang, Y. M., Yang, Y., & Zou, J. L. (2022). Nerve bundle formation during the promotion of peripheral nerve regeneration: collagen VI-neural cell adhesion molecule 1 interaction. *Neural Regen Res*, *17*(5), 1023-1033. https://doi.org/10.4103/1673-5374.324861

Suzumura, A. (2009). [Neurotoxicity by microglia: the mechanisms and potential therapeutic strategy]. *Fukuoka Igaku Zasshi*, *100*(7), 243-247. https://www.ncbi.nlm.nih.gov/pubmed/19764477

Takeuchi, H., Mizuno, T., Zhang, G., Wang, J., Kawanokuchi, J., Kuno, R., & Suzumura, A. (2005). Neuritic beading induced by activated microglia is an early feature of neuronal dysfunction toward neuronal death by inhibition of mitochondrial respiration and axonal transport. *J Biol Chem*, *280*(11), 10444-10454. https://doi.org/10.1074/jbc.M413863200

Tan, Z., Sun, X., Hou, F. S., Oh, H. W., Hilgenberg, L. G., Hol, E. M., van Leeuwen, F. W., Smith, M. A., O'Dowd, D. K., & Schreiber, S. S. (2007). Mutant ubiquitin found in Alzheimer's disease causes neuritic beading of mitochondria in association with neuronal degeneration. *Cell Death Differ*, *14*(10), 1721-1732. https://doi.org/10.1038/sj.cdd.4402180

Tang, L. T., Diaz-Balzac, C. A., Rahman, M., Ramirez-Suarez, N. J., Salzberg, Y., Lazaro-Pena, M. I., & Bulow, H. E. (2019). TIAM-1/GEF can shape somatosensory dendrites independently of its GEF activity by regulating F-actin localization. *Elife*, *8*. https://doi.org/10.7554/eLife.38949

Tao, L., Porto, D., Li, Z., Fechner, S., Lee, S. A., Goodman, M. B., Xu, X. Z. S., Lu, H., & Shen, K. (2019). Parallel Processing of Two Mechanosensory Modalities by a Single Neuron in C. elegans. *Dev Cell*, *51*(5), 617-631.e613. https://doi.org/10.1016/j.devcel.2019.10.008

Tavernarakis, N., Shreffler, W., Wang, S., & Driscoll, M. (1997). unc-8, a DEG/ENaC family member, encodes a subunit of a candidate mechanically gated channel that modulates C. elegans locomotion. *Neuron*, *18*(1), 107-119. https://doi.org/10.1016/s0896-6273(01)80050-7

Taylor, S. R., Santpere, G., Weinreb, A., Barrett, A., Reilly, M. B., Xu, C., Varol, E., Oikonomou, P., Glenwinkel, L., McWhirter, R., Poff, A., Basavaraju, M., Rafi, I., Yemini, E., Cook, S. J., Abrams, A., Vidal, B., Cros, C., Tavazoie, S., Sestan, N., Hammarlund, M., Hobert,

O., & Miller, D. M. (2021). Molecular topography of an entire nervous system. *Cell*, *184*(16), 4329-4347.e4323. https://doi.org/10.1016/j.cell.2021.06.023
Teuscher, A. C., Jongsma, E., Davis, M. N., Statzer, C., Gebauer, J. M., Naba, A., & Ewald, C. Y. (2019). The in-silico characterization of the Caenorhabditis elegans matrisome and proposal of a novel collagen classification. *Matrix Biol Plus*, *1*, 100001. https://doi.org/10.1016/j.mbplus.2018.11.001
Teuscher, A. C., Statzer, C., Goyala, A., Domenig, S. A., Schoen, I., Hess, M., Hofer, A. M., Fossati, A., Vogel, V., Goksel, O., Aebersold, R., & Ewald, C. Y. (2024). Longevity interventions modulate mechanotransduction and extracellular matrix homeostasis in C. elegans. *Nat Commun*, *15*(1), 276. https://doi.org/10.1038/s41467-023-44409-2
Thacker, C., Sheps, J. A., & Rose, A. M. (2006). Caenorhabditis elegans dpy-5 is a cuticle procollagen processed by a proprotein convertase. *Cell Mol Life Sci*, *63*(10), 1193-1204. https://doi.org/10.1007/s00018-006-6012-z
Thein, M. C., McCormack, G., Winter, A. D., Johnstone, I. L., Shoemaker, C. B., & Page, A. P. (2003). Caenorhabditis elegans exoskeleton collagen COL-19: an adult-specific marker for collagen modification and assembly, and the analysis of organismal morphology. *Dev Dyn*, *226*(3), 523-539. https://doi.org/10.1002/dvdy.10259
Thomas, S., Enders, J., Kaiser, A., Rovenstine, L., Heslop, L., Hauser, W., Chadwick, A., & Wright, D. (2023). Abnormal intraepidermal nerve fiber density in disease: A scoping review. *Front Neurol*, *14*, 1161077. https://doi.org/10.3389/fneur.2023.1161077
Toth, M. L., Melentijevic, I., Shah, L., Bhatia, A., Lu, K., Talwar, A., Naji, H., Ibanez-Ventoso, C., Ghose, P., Jevince, A., Xue, J., Herndon, L. A., Bhanot, G., Rongo, C., Hall, D. H., & Driscoll, M. (2012). Neurite sprouting and synapse deterioration in the aging Caenorhabditis elegans nervous system. *J Neurosci*, *32*(26), 8778-8790. https://doi.org/10.1523/JNEUROSCI.1494-11.2012
Tsalik, E. L., Niacaris, T., Wenick, A. S., Pau, K., Avery, L., & Hobert, O. (2003). LIM homeobox gene-dependent expression of biogenic amine receptors in restricted regions of the C. elegans nervous system. *Dev Biol*, *263*(1), 81-102. https://doi.org/10.1016/s0012-1606(03)00447-0
Tu, H., Huhtala, P., Lee, H. M., Adams, J. C., & Pihlajaniemi, T. (2015). Membrane-associated collagens with interrupted triple-helices (MACITs): evolution from a bilaterian common ancestor and functional conservation in C. elegans. *BMC Evol Biol*, *15*, 281. https://doi.org/10.1186/s12862-015-0554-3
Vakkayil, K. L., & Hoppe, T. (2022). Temperature-Dependent Regulation of Proteostasis and Longevity. *Front Aging*, *3*, 853588. https://doi.org/10.3389/fragi.2022.853588
Valdez, G. (2019). Effects of disease-afflicted and aging neurons on the musculoskeletal system. *Bone*, *122*, 31-37. https://doi.org/10.1016/j.bone.2019.01.023
Van de Walle, P., Geens, E., Baggerman, G., Jose Naranjo-Galindo, F., Askjaer, P., Schoofs, L., & Temmerman, L. (2019). CEH-60/PBX regulates vitellogenesis and cuticle permeability through intestinal interaction with UNC-62/MEIS in Caenorhabditis elegans. *PLoS Biol*, *17*(11), e3000499. https://doi.org/10.1371/journal.pbio.3000499
Varani, J., Dame, M. K., Rittie, L., Fligiel, S. E., Kang, S., Fisher, G. J., & Voorhees, J. J. (2006). Decreased collagen production in chronologically aged skin: roles of age-dependent alteration in fibroblast function and defective mechanical stimulation. *Am J Pathol*, *168*(6), 1861-1868. https://doi.org/10.2353/ajpath.2006.051302

Verdú, E., Ceballos, D., Vilches, J. J., & Navarro, X. (2000). Influence of aging on peripheral nerve function and regeneration. *J Peripher Nerv Syst*, *5*(4), 191-208. https://doi.org/10.1046/j.1529-8027.2000.00026.x

Verghese, J., Bieri, P. L., Gellido, C., Schaumburg, H. H., & Herskovitz, S. (2001). Peripheral neuropathy in young-old and old-old patients. *Muscle Nerve*, *24*(11), 1476-1481. https://doi.org/10.1002/mus.1171

Wallace, M. L., Huang, K. W., Hochbaum, D., Hyun, M., Radeljic, G., & Sabatini, B. L. (2020). Anatomical and single-cell transcriptional profiling of the murine habenular complex. *Elife*, *9*. https://doi.org/10.7554/eLife.51271

Wang, H., Zhao, Y., & Zhang, Z. (2019). Age-dependent effects of floxuridine (FUdR) on senescent pathology and mortality in the nematode Caenorhabditis elegans. *Biochem Biophys Res Commun*, *509*(3), 694-699. https://doi.org/10.1016/j.bbrc.2018.12.161

Watson, J. C., & Dyck, P. J. (2015). Peripheral Neuropathy: A Practical Approach to Diagnosis and Symptom Management. *Mayo Clin Proc*, *90*(7), 940-951. https://doi.org/10.1016/j.mayocp.2015.05.004

Way, J. C., & Chalfie, M. (1989). The mec-3 gene of Caenorhabditis elegans requires its own product for maintained expression and is expressed in three neuronal cell types. *Genes Dev*, *3*(12A), 1823-1833. https://doi.org/10.1101/gad.3.12a.1823

White, J. G., Southgate, E., Thomson, J. N., & Brenner, S. (1986). The structure of the nervous system of the nematode Caenorhabditis elegans. *Philos Trans R Soc Lond B Biol Sci*, *314*(1165), 1-340. https://doi.org/10.1098/rstb.1986.0056

Wiesmeier, I. K., Dalin, D., & Maurer, C. (2015). Elderly Use Proprioception Rather than Visual and Vestibular Cues for Postural Motor Control. *Front Aging Neurosci*, *7*, 97. https://doi.org/10.3389/fnagi.2015.00097

Xiao, R., Zhang, B., Dong, Y., Gong, J., Xu, T., Liu, J., & Xu, X. Z. (2013). A genetic program promotes C. elegans longevity at cold temperatures via a thermosensitive TRP channel. *Cell*, *152*(4), 806-817. https://doi.org/10.1016/j.cell.2013.01.020

Yang, W. K., & Chien, C. T. (2019). Beyond being innervated: the epidermis actively shapes sensory dendritic patterning. *Open Biol*, *9*(3), 180257. https://doi.org/10.1098/rsob.180257

Zhu, Y., Li, W., Dong, Y., Xia, C., & Fu, R. (2023). Hemidesmosomes Sense Collagen Damage to Trigger Innate Immune Response in the Epidermis. *Cells*, *12*(18). https://doi.org/10.3390/cells12182223

Ziegenfuss, J. S., & Grueber, W. B. (2013). SAX-7 and menorin light the path for dendrite morphogenesis. *Cell*, *155*(2), 269-271. https://doi.org/10.1016/j.cell.2013.09.029

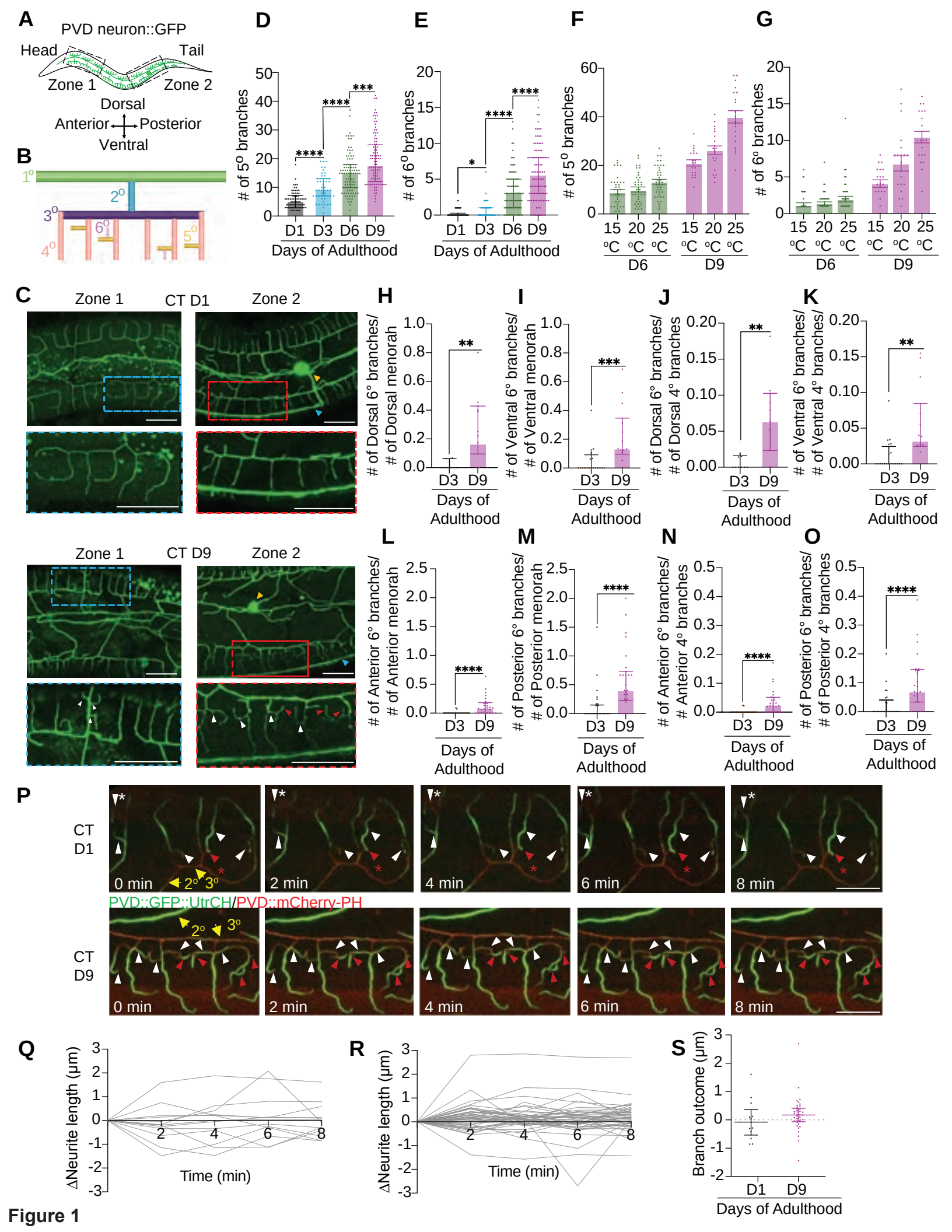
A
PVD neuron::GFP
Head
Tail
Zone 1
Zone 2
Dorsal
Anterior
Posterior
Ventral
B
1°
2°
3°
4°
5°
6°
D
# of 5° branches
D1 D3 D6 D9
Days of Adulthood
E
# of 6° branches
F
# of 5° branches
15 °C 20 °C 25 °C
D6
D9
G
# of 6° branches
C
Zone 1
CT D1
Zone 2
CT D9
H
# of Dorsal 6° branches/ # of Dorsal menorah
I
# of Ventral 6° branches/ # of Ventral menorah
J
# of Dorsal 6° branches/ # of Dorsal 4° branches
K
# of Ventral 6° branches/ # of Ventral 4° branches
L
# of Anterior 6° branches/ # of Anterior menorah
M
# of Posterior 6° branches/ # of Posterior menorah
N
# of Anterior 6° branches/ # of Anterior 4° branches
O
# of Posterior 6° branches/ # of Posterior 4° branches
D3 D9
Days of Adulthood
P
CT D1
CT D9
0 min
2 min
4 min
6 min
8 min
PVD::GFP::UtrCH/PVD::mCherry-PH
Q
ΔNeurite length (μm)
Time (min)
R
S
Branch outcome (μm)
D1 D9
Days of Adulthood

Figure 1

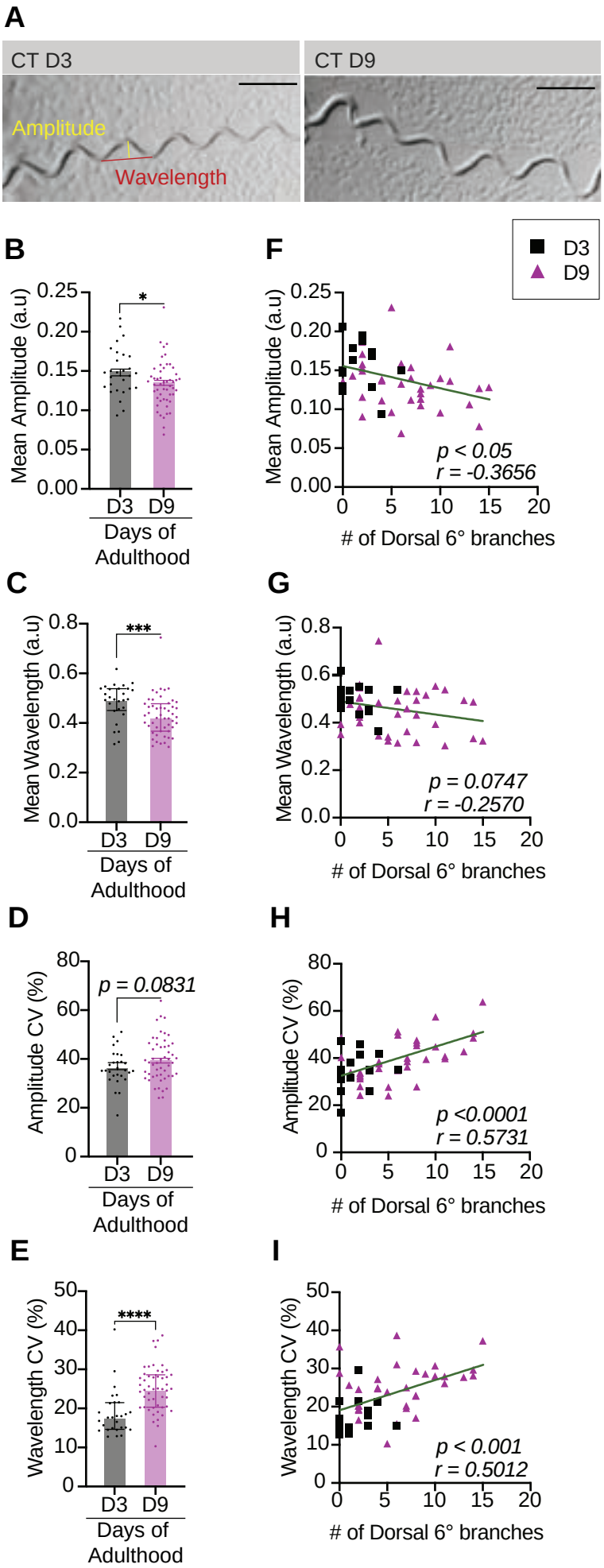
A
CT D3
CT D9
Amplitude
Wavelength
B
Mean Amplitude (a.u)
0.25
0.20
0.15
0.10
0.05
0.00
*
D3
D9
Days of Adulthood
F
D3
D9
Mean Amplitude (a.u)
p < 0.05
r = -0.3656
# of Dorsal 6° branches
C
Mean Wavelength (a.u)
0.8
0.6
0.4
0.2
0.0
***
D3
D9
Days of Adulthood
G
Mean Wavelength (a.u)
p = 0.0747
r = -0.2570
# of Dorsal 6° branches
D
Amplitude CV (%)
80
60
40
20
0
p = 0.0831
D3
D9
Days of Adulthood
H
Amplitude CV (%)
p <0.0001
r = 0.5731
# of Dorsal 6° branches
E
Wavelength CV (%)
50
40
30
20
10
0
****
D3
D9
Days of Adulthood
I
Wavelength CV (%)
p < 0.001
r = 0.5012
# of Dorsal 6° branches

Figure 2

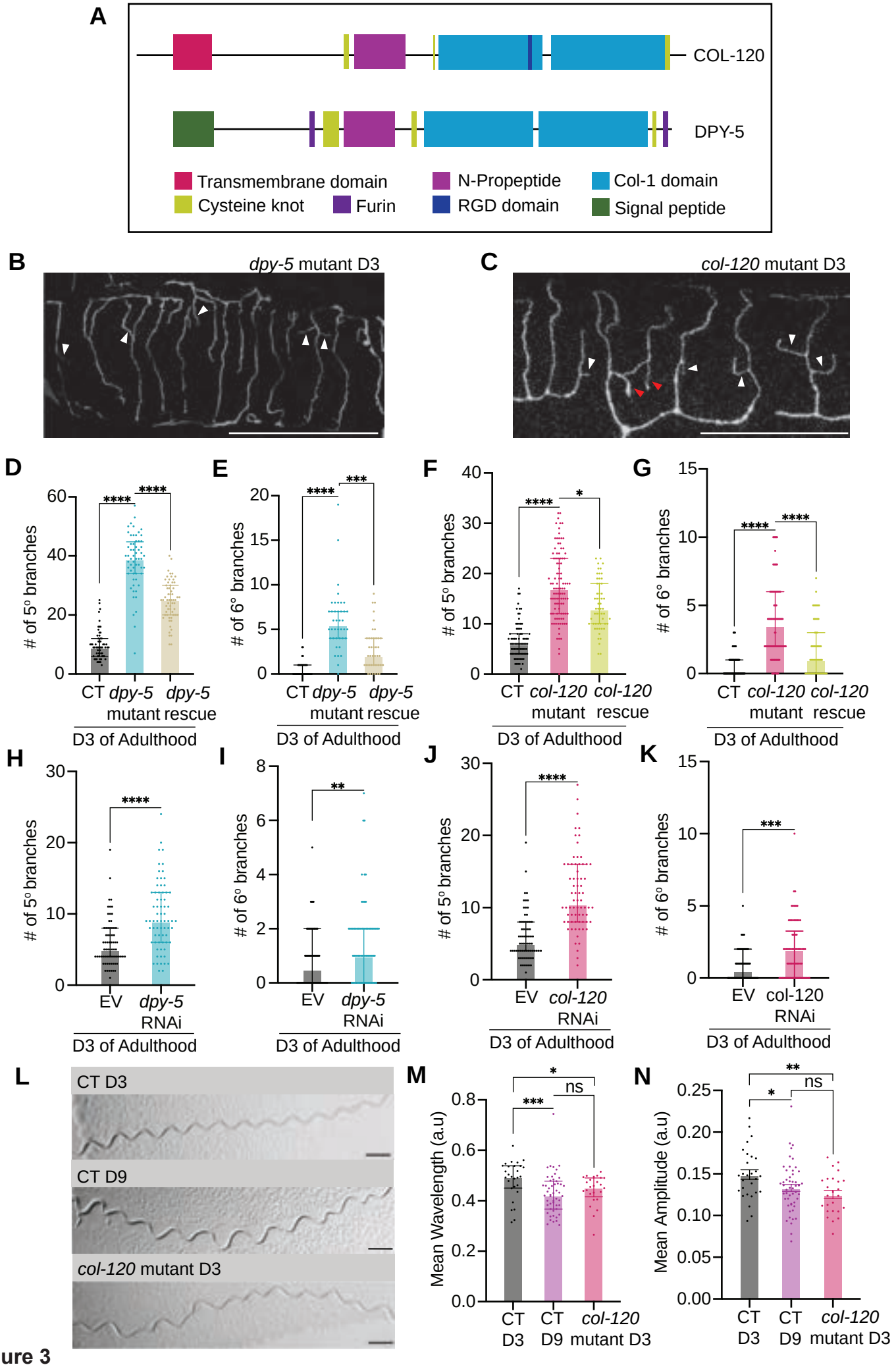
A
COL-120
DPY-5
Transmembrane domain
Cysteine knot
Furin
N-Propeptide
RGD domain
Col-1 domain
Signal peptide
B
dpy-5 mutant D3
C
col-120 mutant D3
D
# of 5° branches
CT
dpy-5 mutant
dpy-5 rescue
D3 of Adulthood
E
# of 6° branches
F
col-120 mutant
col-120 rescue
G
H
EV
dpy-5 RNAi
I
J
col-120 RNAi
K
L
CT D3
CT D9
col-120 mutant D3
M
Mean Wavelength (a.u)
ns
N
Mean Amplitude (a.u)

Figure 3

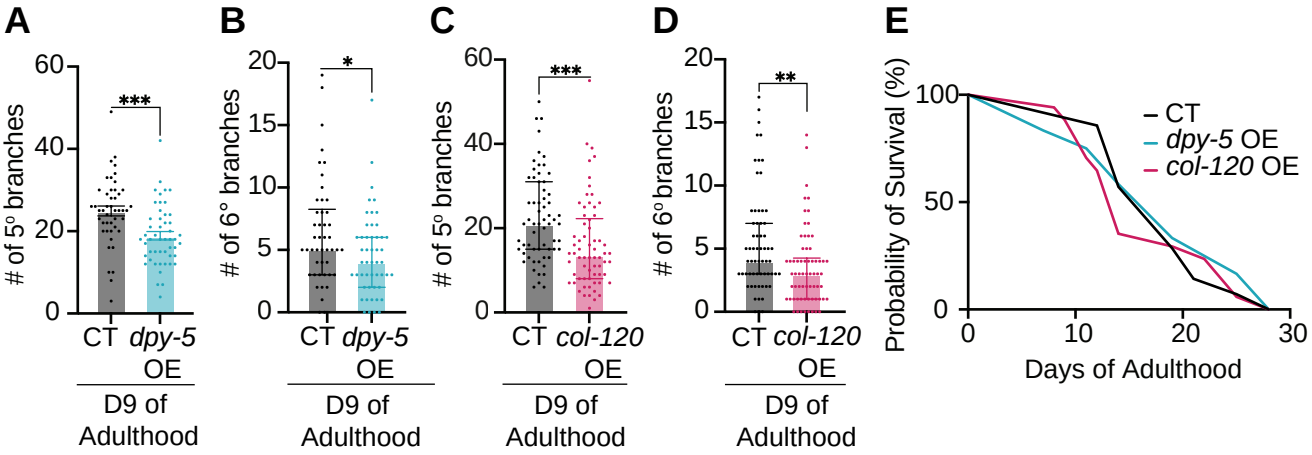
A
B
C
D
E
# of 5° branches
# of 6° branches
***
*
**
CT
dpy-5 OE
col-120 OE
D9 of Adulthood
Probability of Survival (%)
Days of Adulthood
CT
dpy-5 OE
col-120 OE

Figure 4

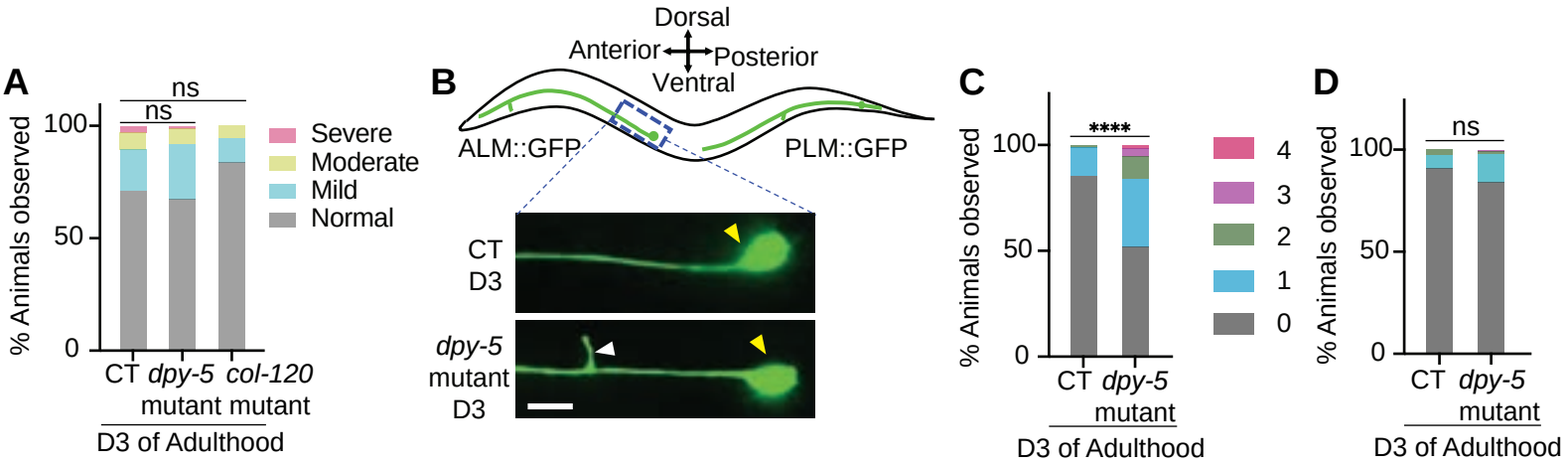
A
ns
ns
100
50
0
% Animals observed
Severe
Moderate
Mild
Normal
CT
dpy-5 mutant
col-120 mutant
D3 of Adulthood
B
Dorsal
Anterior
Posterior
Ventral
ALM::GFP
PLM::GFP
CT D3
dpy-5 mutant D3
C
****
100
50
0
% Animals observed
4
3
2
1
0
CT
dpy-5 mutant
D3 of Adulthood
D
ns
100
50
0
% Animals observed
CT
dpy-5 mutant
D3 of Adulthood

Figure 5

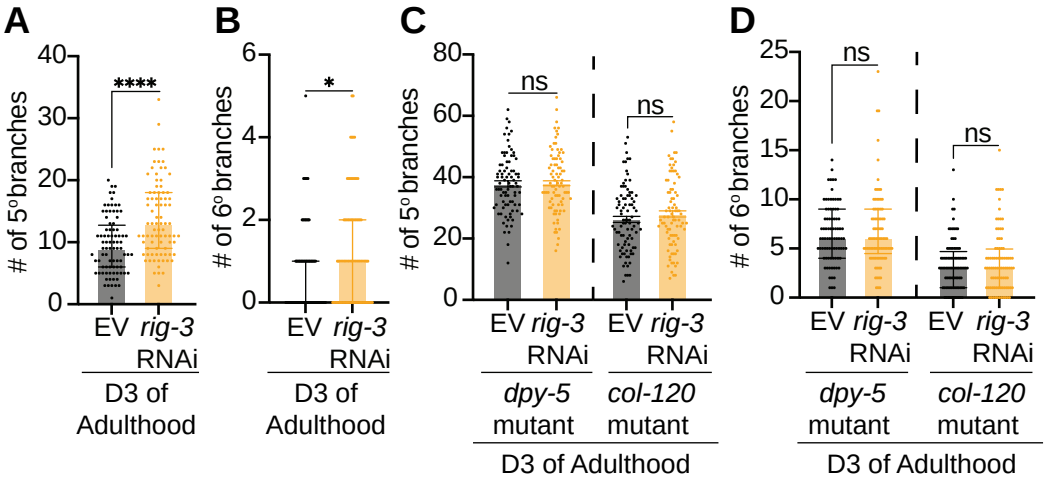
A
B
C
D
# of 5° branches
# of 6° branches
****
*
ns
EV
rig-3 RNAi
D3 of Adulthood
dpy-5 mutant
col-120 mutant

Figure 6

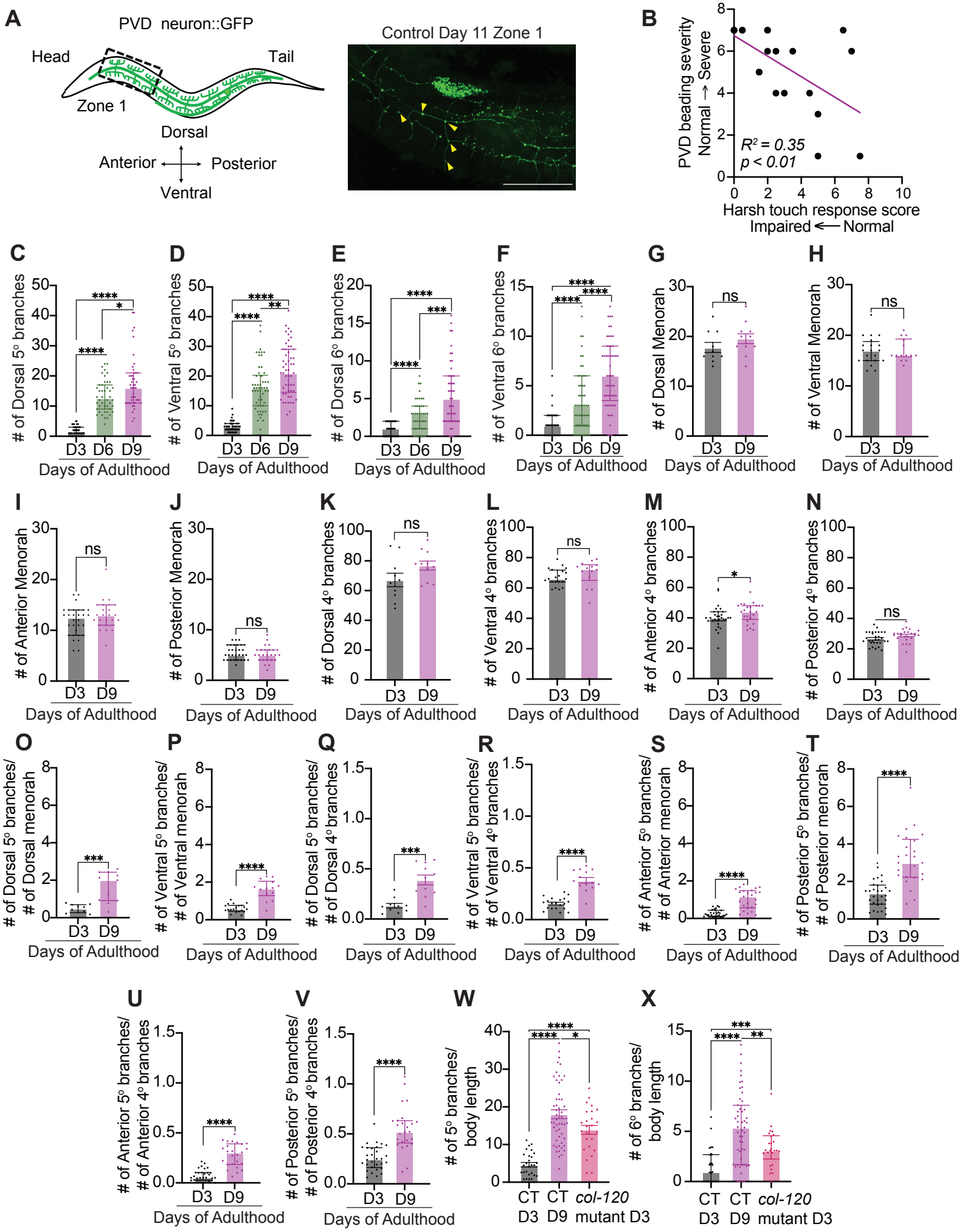
A
PVD neuron::GFP
Head
Tail
Zone 1
Dorsal
Anterior
Posterior
Ventral
Control Day 11 Zone 1
B
PVD beading severity
Normal → Severe
$R^2 = 0.35$
$p < 0.01$
Harsh touch response score
Impaired ← Normal
C
# of Dorsal 5° branches
D
# of Ventral 5° branches
E
# of Dorsal 6° branches
F
# of Ventral 6° branches
G
# of Dorsal Menorah
H
# of Ventral Menorah
I
# of Anterior Menorah
J
# of Posterior Menorah
K
# of Dorsal 4° branches
L
# of Ventral 4° branches
M
# of Anterior 4° branches
N
# of Posterior 4° branches
O
# of Dorsal 5° branches/ # of Dorsal menorah
P
# of Ventral 5° branches/ # of Ventral menorah
Q
# of Dorsal 5° branches/ # of Dorsal 4° branches
R
# of Ventral 5° branches/ # of Ventral 4° branches
S
# of Anterior 5° branches/ # of Anterior menorah
T
# of Posterior 5° branches/ # of Posterior menorah
U
# of Anterior 5° branches/ # of Anterior 4° branches
V
# of Posterior 5° branches/ # of Posterior 4° branches
W
# of 5° branches/ body length
X
# of 6° branches/ body length
D3
D6
D9
Days of Adulthood
CT D3
CT D9
col-120 mutant D3
ns

Figure S1

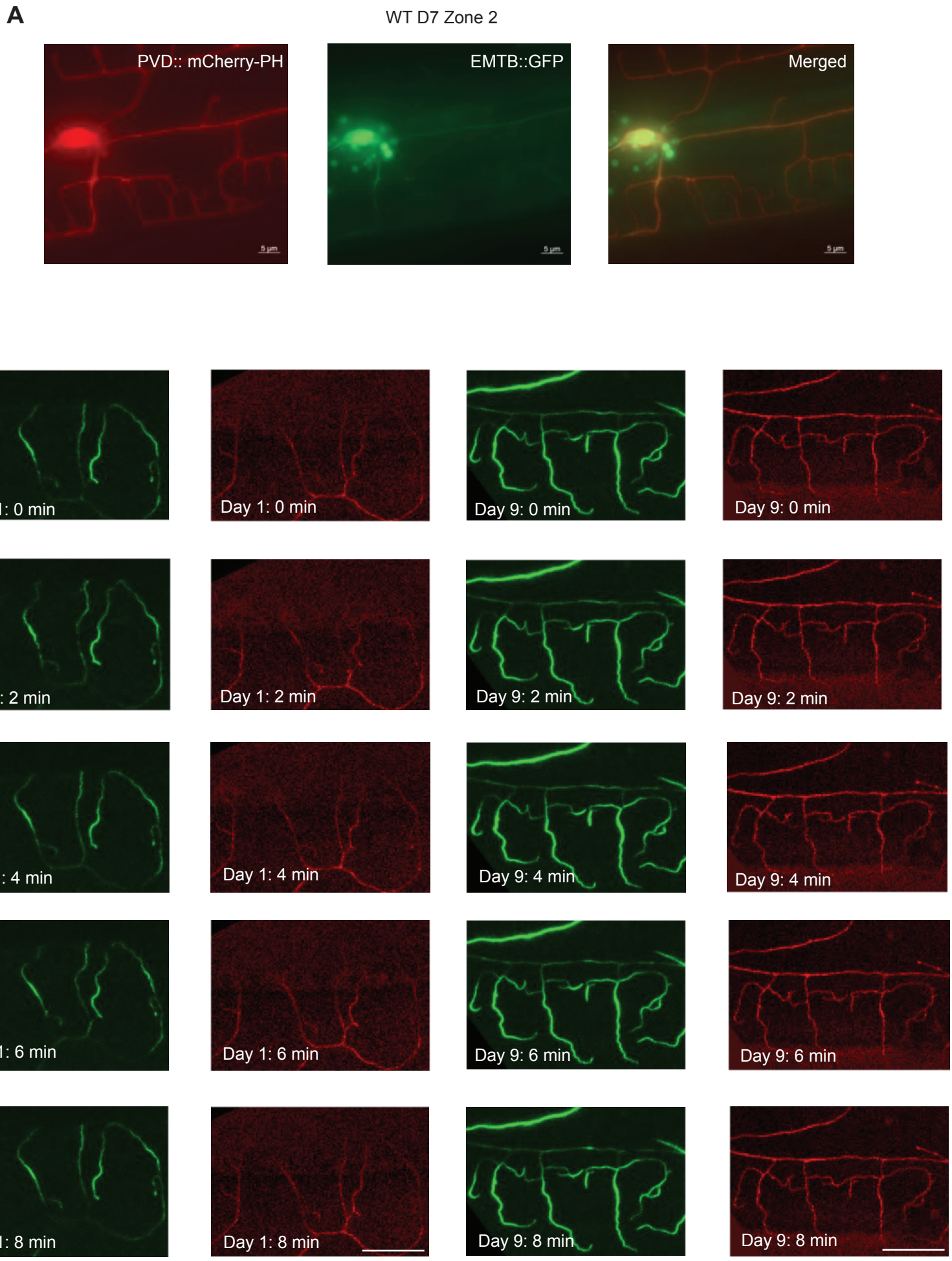
A
WT D7 Zone 2
PVD:: mCherry-PH
EMTB::GFP
Merged
B
Day 1: 0 min
Day 1: 0 min
Day 9: 0 min
Day 9: 0 min
Day 1: 2 min
Day 1: 2 min
Day 9: 2 min
Day 9: 2 min
Day 1: 4 min
Day 1: 4 min
Day 9: 4 min
Day 9: 4 min
Day 1: 6 min
Day 1: 6 min
Day 9: 6 min
Day 9: 6 min
Day 1: 8 min
Day 1: 8 min
Day 9: 8 min
Day 9: 8 min

Figure S2

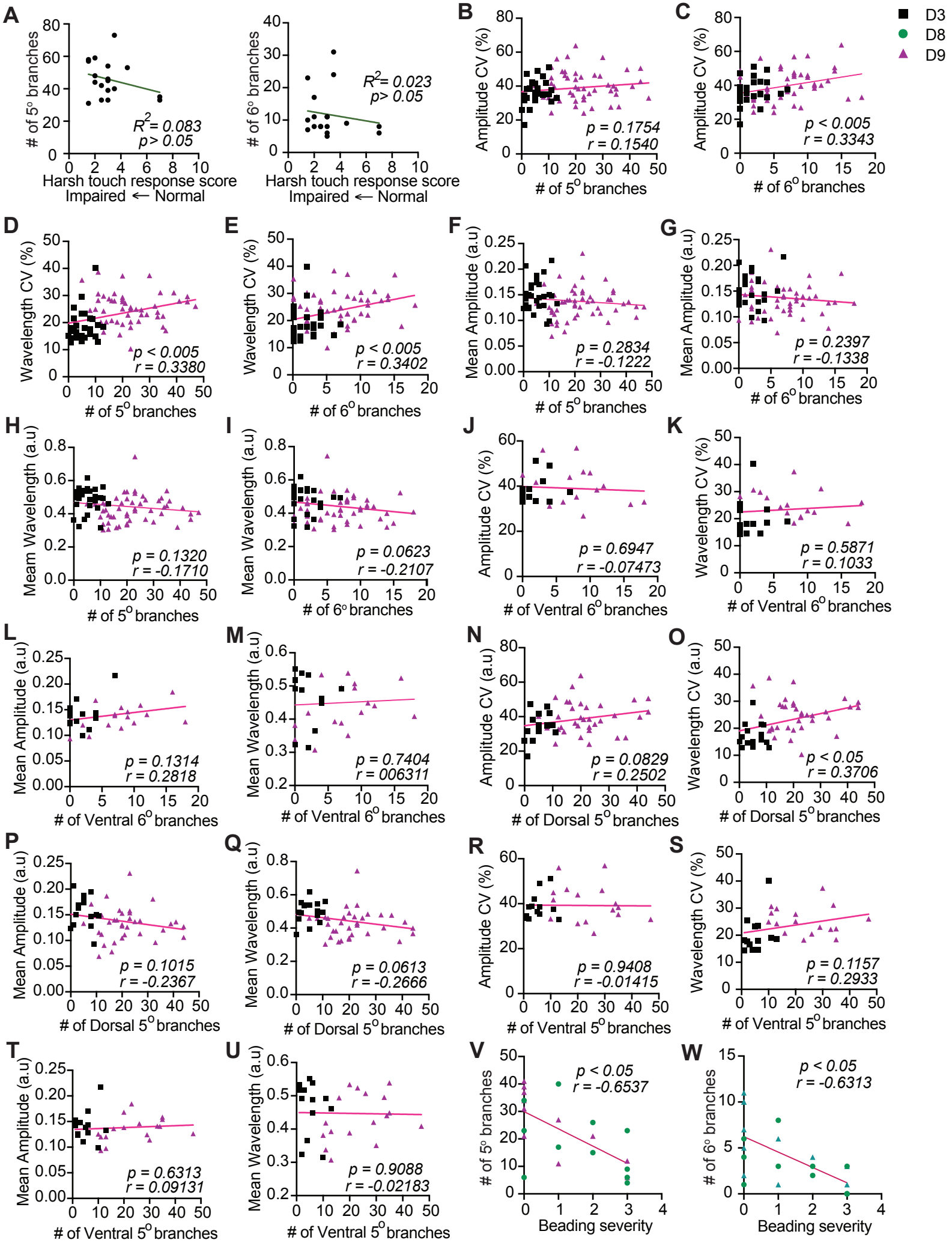
A
# of 5° branches
R^2= 0.083
p> 0.05
Harsh touch response score
Impaired ← Normal
# of 6° branches
R^2= 0.023
p> 0.05
Harsh touch response score
Impaired ← Normal
B
Amplitude CV (%)
p = 0.1754
r = 0.1540
# of 5° branches
C
Amplitude CV (%)
p < 0.005
r = 0.3343
# of 6° branches
D3
D8
D9
D
Wavelength CV (%)
p < 0.005
r = 0.3380
# of 5° branches
E
Wavelength CV (%)
p < 0.005
r = 0.3402
# of 6° branches
F
Mean Amplitude (a.u)
p = 0.2834
r = -0.1222
# of 5° branches
G
Mean Amplitude (a.u)
p = 0.2397
r = -0.1338
# of 6° branches
H
Meam Wavelength (a.u)
p = 0.1320
r = -0.1710
# of 5° branches
I
Mean Wavelength (a.u)
p = 0.0623
r = -0.2107
# of 6° branches
J
Amplitude CV (%)
p = 0.6947
r = -0.07473
# of Ventral 6° branches
K
Wavelength CV (%)
p = 0.5871
r = 0.1033
# of Ventral 6° branches
L
Mean Amplitude (a.u)
p = 0.1314
r = 0.2818
# of Ventral 6° branches
M
Mean Wavelength (a.u)
p = 0.7404
r = 006311
# of Ventral 6° branches
N
Amplitude CV (a.u)
p = 0.0829
r = 0.2502
# of Dorsal 5° branches
O
Wavelength CV (a.u)
p < 0.05
r = 0.3706
# of Dorsal 5° branches
P
Mean Amplitude (a.u)
p = 0.1015
r = -0.2367
# of Dorsal 5° branches
Q
Mean Wavelength (a.u)
p = 0.0613
r = -0.2666
# of Dorsal 5° branches
R
Amplitude CV (%)
p = 0.9408
r = -0.01415
# of Ventral 5° branches
S
Wavelength CV (%)
p = 0.1157
r = 0.2933
# of Ventral 5° branches
T
Mean Amplitude (a.u)
p = 0.6313
r = 0.09131
# of Ventral 5° branches
U
Mean Wavelength (a.u)
p = 0.9088
r = -0.02183
# of Ventral 5° branches
V
# of 5° branches
p < 0.05
r = -0.6537
Beading severity
W
# of 6° branches
p < 0.05
r = -0.6313
Beading severity

Figure S3

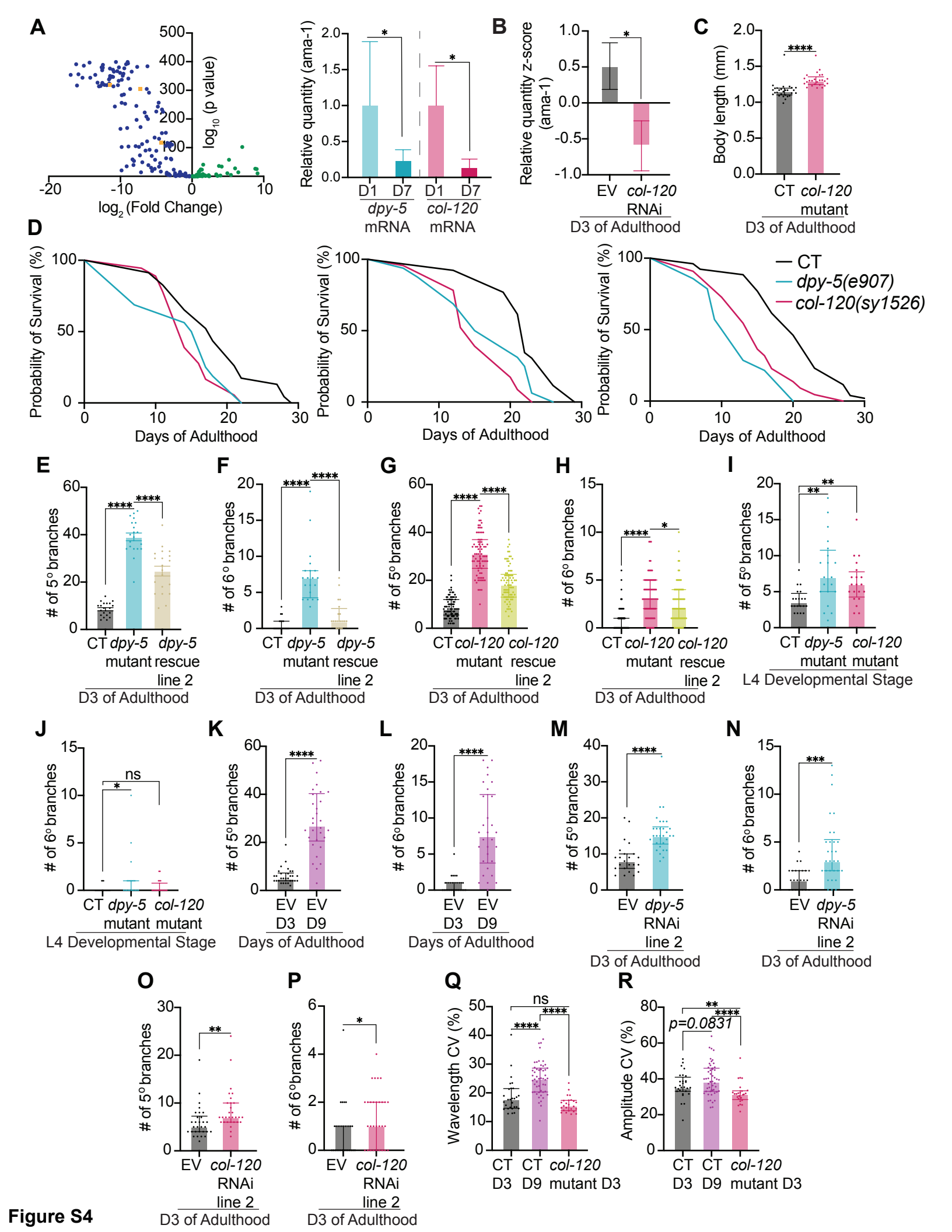
A
log10 (p value)
log2 (Fold Change)
Relative quantity (ama-1)
D1 D7 D1 D7
dpy-5 mRNA
col-120 mRNA
B
Relative quantity z-score (ama-1)
EV col-120 RNAi
D3 of Adulthood
C
Body length (mm)
CT col-120 mutant
D3 of Adulthood
D
Probability of Survival (%)
Days of Adulthood
CT
dpy-5(e907)
col-120(sy1526)
E
# of 5° branches
CT dpy-5 mutant dpy-5 rescue line 2
D3 of Adulthood
F
# of 6° branches
CT dpy-5 mutant dpy-5 rescue line 2
D3 of Adulthood
G
# of 5° branches
CT col-120 mutant col-120 rescue line 2
D3 of Adulthood
H
# of 6° branches
CT col-120 mutant col-120 rescue line 2
D3 of Adulthood
I
# of 5° branches
CT dpy-5 mutant col-120 mutant
L4 Developmental Stage
J
# of 6° branches
ns
CT dpy-5 mutant col-120 mutant
L4 Developmental Stage
K
# of 5° branches
EV D3 EV D9
Days of Adulthood
L
# of 6° branches
EV D3 EV D9
Days of Adulthood
M
# of 5° branches
EV dpy-5 RNAi line 2
D3 of Adulthood
N
# of 6° branches
EV dpy-5 RNAi line 2
D3 of Adulthood
O
# of 5° branches
EV col-120 RNAi line 2
D3 of Adulthood
P
# of 6° branches
EV col-120 RNAi line 2
D3 of Adulthood
Q
Wavelength CV (%)
ns
CT D3 CT D9 col-120 mutant D3
R
Amplitude CV (%)
p=0.0831
CT D3 CT D9 col-120 mutant D3

Figure S4

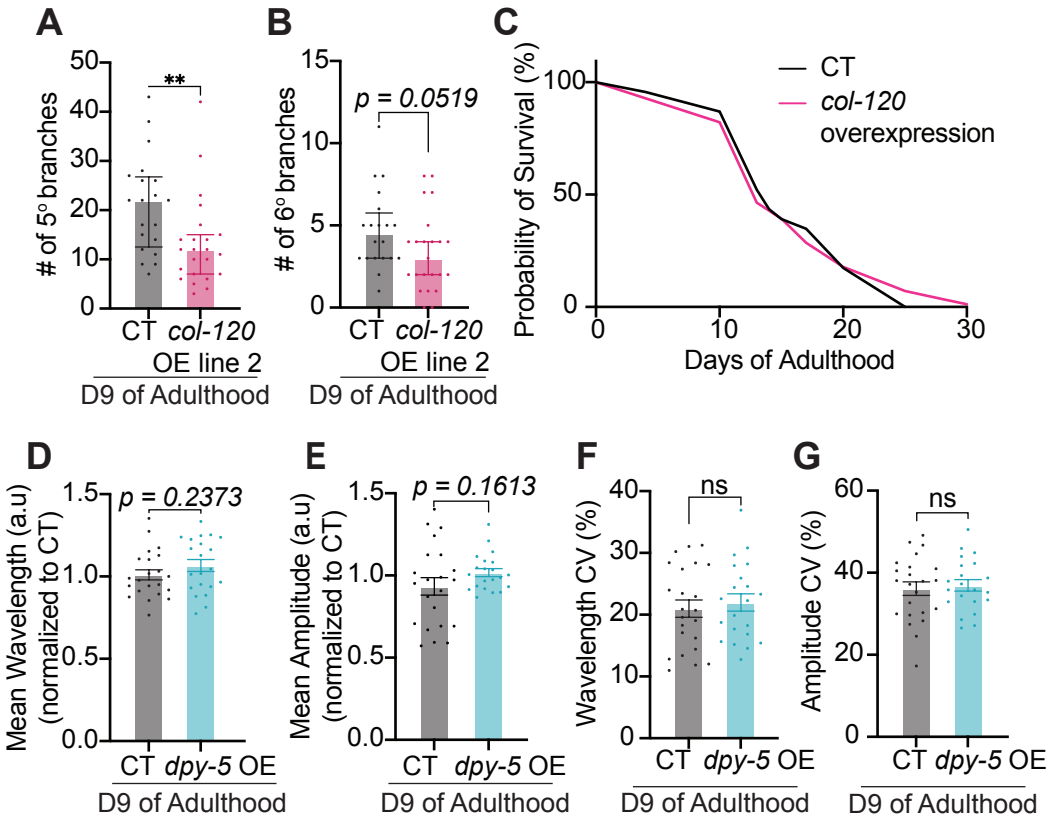
A
B
C
# of 5° branches
# of 6° branches
**
p = 0.0519
CT
col-120
OE line 2
D9 of Adulthood
Probability of Survival (%)
CT
col-120
overexpression
Days of Adulthood
D
E
F
G
Mean Wavelength (a.u) (normalized to CT)
Mean Amplitude (a.u) (normalized to CT)
Wavelength CV (%)
Amplitude CV (%)
p = 0.2373
p = 0.1613
ns
dpy-5 OE

Figure S5

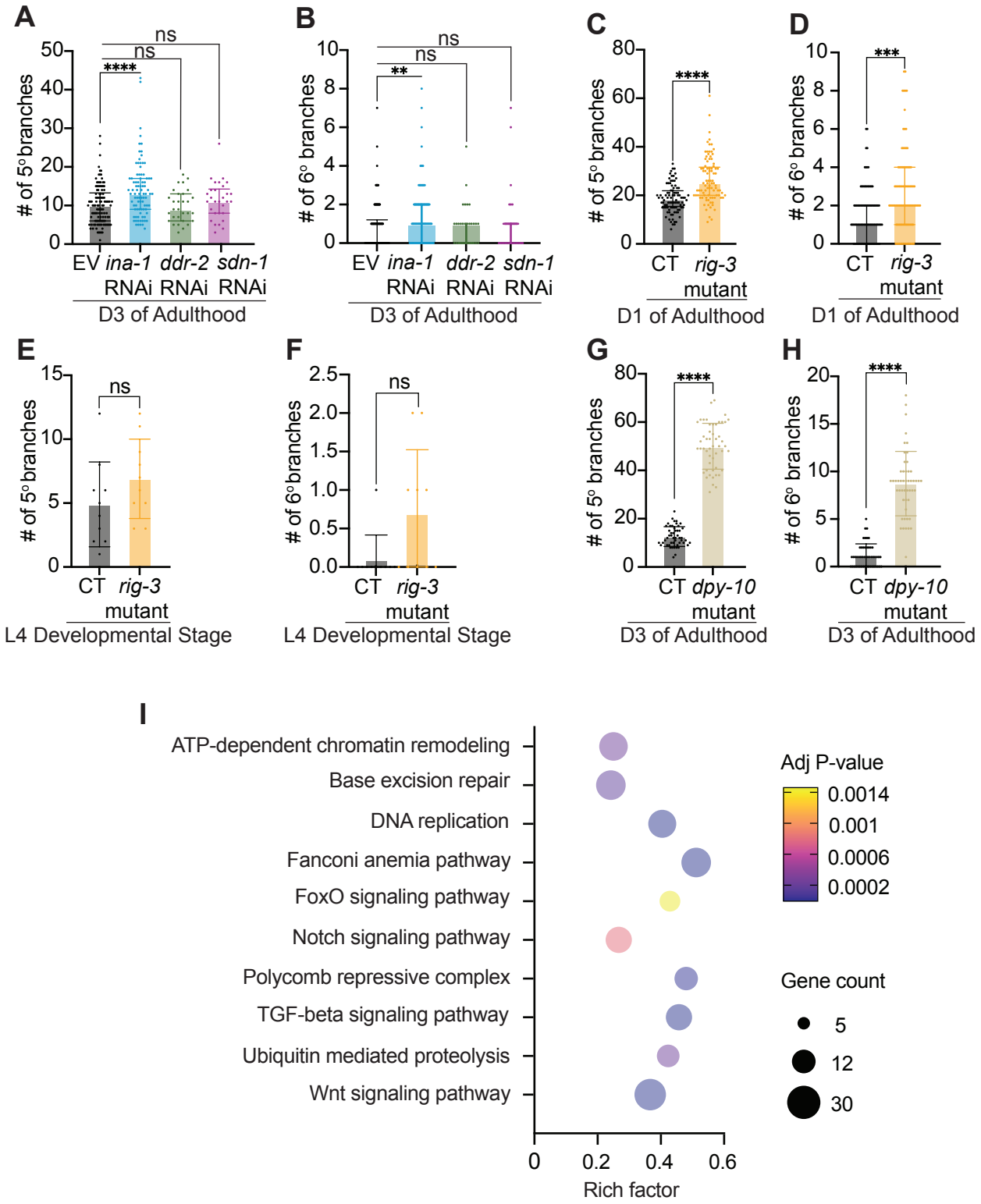
A
# of 5° branches
ns
ns
****
EV
ina-1 RNAi
ddr-2 RNAi
sdn-1 RNAi
D3 of Adulthood
B
# of 6° branches
ns
ns
**
EV
ina-1 RNAi
ddr-2 RNAi
sdn-1 RNAi
D3 of Adulthood
C
# of 5° branches
****
CT
rig-3 mutant
D1 of Adulthood
D
# of 6° branches
***
CT
rig-3 mutant
D1 of Adulthood
E
# of 5° branches
ns
CT
rig-3 mutant
L4 Developmental Stage
F
# of 6° branches
ns
CT
rig-3 mutant
L4 Developmental Stage
G
# of 5° branches
****
CT
dpy-10 mutant
D3 of Adulthood
H
# of 6° branches
****
CT
dpy-10 mutant
D3 of Adulthood
I
ATP-dependent chromatin remodeling
Base excision repair
DNA replication
Fanconi anemia pathway
FoxO signaling pathway
Notch signaling pathway
Polycomb repressive complex
TGF-beta signaling pathway
Ubiquitin mediated proteolysis
Wnt signaling pathway
Rich factor
Adj P-value
0.0014
0.001
0.0006
0.0002
Gene count
5
12
30

Figure S6

Difference	Right 5th branches	Left 5th branches	Right 6th branches	Left 6th branches
WT D3 vs WT D6	+14 ****	+10 ****	+2 ****	+1 ***
WT D6 vs WT D9	+3.208 *	+4 *	+3.5 ****	+3.5 ****
WT D3 vs WT D9	+18 ****	+14 ****	+4.5 ****	+4.5 ****

Table S1